NUMERICAL ANALYSIS OF IMMERSION COOLING ON A SERVER USING AL2O3/MINERAL OIL NANOFLUID

By

PRAJWAL SRINIVAS MURTHY

Presented to the Faculty of the Graduate School of

The University of Texas at Arlington in Partial Fulfillment

Of the Requirements

For the Degree of

MASTER OF SCIENCE IN MECHANICAL ENGINEERING

THE UNIVERSITY OF TEXAS AT ARLINGTON

August 2020

Copyright © by Prajwal Srinivas Murthy 2020

All Rights Reserved

ACKNOWLEDGEMENTS

I would like to express my sincere gratitude to Dr. Dereje Agonafer for his incessant support, motivation and encouragement for over one and a half years with my research. I would also like to thank him for reviewing my work and offering me tips on further improving the current study, and for being a part of my thesis defense. I am also extremely grateful towards him for presenting me an opportunity for writing a paper for my current work and presenting it at conferences.

I would like to thank Dr. Amaya Miguel and Dr. Haji Sheikh for taking the time out of their busy schedule and being a part of my thesis committee.

I would like to thank Dr. Amirreza Niazmand, Mr. Satyam Saini, Mr. Pardeep Shahi and Mr. Pratik Bansode for being my mentors and guiding me throughout my work to achieve valuable results and put up a great presentation.

I would like to thank all my friends in the EMNSPC group for being a part of my thesis defense and offering me the moral support to showcase my work.

My special thanks to my parents, Mr. Srinivas Keshava Murthy and Mrs. Vathsala Murthy, and my dear friends for offering me that unconditional love and a strong support to help me achieve my goals. I am forever obliged to have them in my life and wish to continue making them proud.

August 10, 2020

Abstract

NUMERICAL ANALYSIS OF IMMERSION COOLING ON A SERVER USING AL2O3/MINERAL OIL NANOFLUID

(Reprinted with permission © 2020 ASME) [38]

PRAJWAL SRINIVAS MURTHY, MS

The University of Texas at Arlington, 2020

Supervising Professor: Dr. Dereje Agonafer

In the current world, technology has developed significantly, with a massive processing and storage of data, resulting in the high increase in Power Density and Heat Generation of servers, computers and its components in data centers. This calls for an engineering solution, for efficient heat dissipation of these servers to ensure their reliability and prolonged working. Air cooling is a prominent method of data center cooling. However, due to its low heat carrying capacity, it is not an efficient method for cooling high heat generating servers. There are two methods to remove this heat, increasing the area of heat transfer being one of the methods, which is not feasible everywhere. To tackle this problem, liquid immersion cooling method has emerged as a prominent method for cooling servers and its components in data centers, where the servers can directly be immersed inside the liquid, making the process simpler and cost effective. Water has

higher thermal properties like heat capacity, but the limitation is that the liquid must be dielectric to save equipment from short-circuit. This feature also influences the thermal conductivity of the liquids. Generally dielectric liquids have low thermal conductivity which affects the thermal performance of the cooling process. Thermal conductivity of the dielectric liquids is drastically increased with the introduction of nano particles, which has proven to be the best method.

Nano particles are metal and non-metal particles with the size between 1 to 150 nanometers. To keep the dielectric feature of the liquid, the non-metallic nano particle can be added to the liquid. Therefore, the Alumina which is one of the materials using as an electrical insulation is used. The mean size of the nano particle used in this work is 80 nm and the liquid are mineral oil, which is a low-price liquid for immersion cooling compared to other dielectric liquids. The concentration of nano particles was 0 to 5 percent and it is assumed to remain homogeneous. The properties of the mixture were calculated based on the theoretical formula and it was function of temperature. In this work, we simulated heat transfer and effect of the nano particle concentration on the junction temperature of the processors using CFD techniques. The chosen server is an open compute server which has two processor in a row. The server was modelled in Ansys Icepack and simulations were performed for pure mineral oil and nanofluid at particle concentrations of 1%, 3% and 5 % at 1, 2 and 3 LPM respectively. Prior to the study, effect of frame height on the maximum CPU junction temperature was tested using pure mineral oil. Drastic reduction in maximum CPU temperature was observed with a smaller frame height and this height was maintained throughout the study. Simulations were conducted for 3 different heatsink geometries, namely parallel plate, cylindrical bonded pin and plate

fin heatsink. From results obtained, effect of nanoparticle concentration on the maximum CPU junction temperature, pressure drop and pumping power were studied and comparisons were made for different nanoparticle concentration and flow rates. Also, comparisons on CPU junction temperature, pressure drop, and pumping power obtained from simulations using the 3 different heatsink geometries were made.

TABLE OF CONTENTS

ACKNOWLEDGEMENTS iii

Abstract iv

List of Illustrations x

Chapter 1 1

INTRODUCTION 1

1.1 Data Centers and Computers 1

1.2 Air cooling of data servers: 2

1.3 Liquid Cooling of data servers: 4

1.4 Indirect liquid cooling 4

1.5 Direct liquid cooling 6

Chapter 2 10

MOTIVATION AND OBJECTIVE 10

Chapter 3 13

GEOMETRY, METHODS AND FORMULA 13

3.1 Server Description 13

3.2 Boundary Conditions 14

3.3 Properties of the Nanofluid 15

3.4 Thermal Conductivity and Specific Heat 17

3.5 Governing Equations 20

3.6 Heatsinks ... 21

3.7 Optimization of Heatsinks: ... 22

3.8 Mesh Sensitivity Analysis ... 25

3.9 Effect of cabinet height on CPU temperature: ... 26

Chapter 4 ... 30

RESULTS AND DISCUSSION ... 30

4.1 Effect of nanoparticle concentration and flow rate on the maximum CPU junction temperature and pressure drop for the parallel plate heatsink configuration: ... 30

4.2 Effect of nanoparticle concentration and flow rate on the maximum CPU junction temperature and pressure drop for the pin fin heatsink configuration: ... 33

4.3 Effect of nanoparticle concentration and flow rate on the maximum CPU junction temperature and pressure drop for the plate fin heatsink configuration: ... 35

4.4 Pumping Power for the 3 Heatsink geometries: ... 38

4.5 Percentage increase in pumping power for the 3 heatsink geometries between 0 and 5 mass% of Al2O3: ... 42

Chapter 5 ... 45

CONCLUSION AND FUTURE SCOPE ... 45

REFERENCES ... 47

List of Tables

Table 1: Properties of pure mineral oil 16

Table 2: Physical properties of AL2O3 [34] 17

Table 3: Thermal conductivity and specific heat 40 ℃ 20

Table 4: Dimensions of the baseline model of the parallel plate heatsink [25] 22

Table 5: Dimensions of the optimized model of the parallel plate heatsink 23

Table 6: Dimensions of the Pin Fin Heatsink [25] 24

Table 7: Dimensions of the plate fin heatsink [25] 25

Table 8: Pumping Power for the parallel plate heatsink geometry: 39

Table 9: Pumping Power for the pin fin heatsink geometry: 40

Table 10: Pumping Power for the plate fin heatsink geometry: 41

Table 11: Percentage increase in pumping power for the 3 heatsink geometries 43

List of Illustrations

Figure 1-1: Air cooled data center 3

Figure 1-2: Cold Plate [25] 5

Figure 1-3: Dielectric cooled server [25] 6

Figure 1-4: Schematic of an immersion cooled system [9] 7

Figure 1-5: Single-Phase immersion cooling [25] 8

Figure 1-6: Two-Phase immersion cooling [25] 9

Figure 3-1: Baseline model of the immersion cooled server 13

Figure 3-2: The 3rd generation open commute server using in the current study 14

Figure 3-3: Boundary conditions for the baseline model 15

Figure 3-4: Variation of thermal conductivity with temperature at 0 and 5 mass% of Al2O3 18

Figure 3-5: Variation of specific heat with temperature at 0 and 5 mass% of Al2O3 18

Figure 3-6: Baseline model of the parallel plate heatsink [25] 22

Figure 3-7: Optimized model of the pin fin heatsink [25] 23

Figure 3-8: Optimized model of the plate fin heatsink [25] 24

Figure 3-9: Mesh Sensitivity Analysis 27

Figure 3-10: CPU temperature with standard frame height 27

Figure 3-11: CPU temperature with reduced frame height 28

Figure 3-12: Velocity profile with standard frame height 29

Figure 3-13: Velocity profile with reduced frame height 29

Figure 4-1: Variation of CPU Tmax with flow rate at different mass% of Al2O3 for parallel plate heatsink geometry 30

Figure 4-2: Variation of Pdrop with flow rate at different mass% of Al2O3 for parallel plate heatsink geometry 32

Figure 4-3: Variation of CPU Tmax with flow rate at different mass% of Al2O3 for pin fin heatsink geometry 33

Figure 4-4: Variation of Pdrop with flow rate at different mass% of Al2O3 for pin heatsink geometry 34

Figure 4-5: Variation of CPU Tmax with flow rate at different mass% of Al2O3 for plate fin heatsink geometry 35

Figure 4-6: Variation of Pdrop with flow rate at different mass% of Al2O3 for plate fin heatsink geometry 37

Chapter 1

INTRODUCTION

1.1 Data Centers and Computers

The data center is a dedicated space in an industry that houses the servers mounted in racks, where the generated data is stored, managed, and disseminated accordingly. The most critical systems of networks are housed in data centers, ensuring the continuity of daily operations [1], [2]. In the current world, rapid technological growth has resulted in a paradigm shift, with increased demand towards computer applications in industries and sectors like education, healthcare, and finance. Tons of data, services and applications contained in a data center that are accessed, produced and disseminated daily, are a focal point for the continuity of operation of these industries and sectors, for their betterment and growth. Online content is accessed and stored by million users, along with large and medium enterprises on the World Wide Web [3]. This ever-increasing demand posits drawbacks, manifested in the increase in power density and heat generation of servers and electronic components at rack level, with considerable energy consumption by the data centers. Hence, removing the generated heat is one of the biggest concerns faced, to maintain the safe and reliable operation of servers in data centers. Also, constant increase in the data center cooling costs due to continual increase in demand towards data centers posits another issue. With an improvement in semiconductor technologies, IT load is expected to increase, necessitating an efficient data center cooling method [4], [5]. Survey has shown the increased consumption of energy by data centers during the recent years, with data center cooling costs accelerating on a day to day basis. The United States Department of Energy in

collaboration with Lawrence Berkeley National Laboratory have reported the consumption of 70 billion kWh of energy by data centers in 2014, which represents 2% of the country's total energy consumption, accounting for 40% of the total energy's bill [6],[7]. To ensure safe and reliable working of data centers, it is imperative to opt for an efficient method of data center cooling that achieves the objectives of efficient dissipation of generated heat, also keeping the reduction in the cost of data center cooling in mind. To achieve these objectives:

The following two methods are the commonly used methods of data center cooling:

1. Air Cooling
2. Liquid Cooling

1.2 Air cooling of data servers:

In this method, air is used as the cooling medium for the dissipation of generated heat. This method works the convective mode of heat transfer, where the forced convection of air over the heatsinks dissipates the generated heat. The Heatsinks are mounted on the processors, and they aid in transferring the heat generated in processors to the outside medium. The axial fans regulate the airflow from inlet to the outlet, which is passed based on the generated heat of the servers. The airflow carries the heat from inlet to the outlet. The hot air exiting the server outlet enters the hot aisle, rises, and is directed into Computer Room Air Conditioning (CRAC) unit, and air is cooled down to the essential temperature. The cooled air is then sent to the cold aisle. Figure 1-1 shows the processes of air cooling in data centers. Air has poor limitations to cool high powered packages. Firstly, air has poor thermal conductivity and specific heat capacity, making it inadequate

to adopt air cooling as the method of data center cooling for high temperature application. Also, additional number of fins on the heatsinks are required to maximize the surface area for enhanced heat transfer. This increases the material cost and complexity of the cooling process. Also, large space is occupied to accommodate ducting systems and fans, and thus makes the setup more complex and expensive. ASHRAE (American Society of Heating, Refrigeration and Air-Conditioning Engineers) has defined an Air-Side Economizer (ASE) consisting of a duct, damper, and an automatic cooling system that works in conjunction with the cooling system to eliminate the requirement for mechanical cooling, by supplying outside cool air for data center cooling. However, the temperature and humidity must be within the specified levels of 35-45 °C inlet temperature. Also, high overhead costs associated with the filters and installation of dehumidification devices, and requirement of the entry of particulate and gaseous contaminants to be within allowable standards pose another problem [4]-[6].

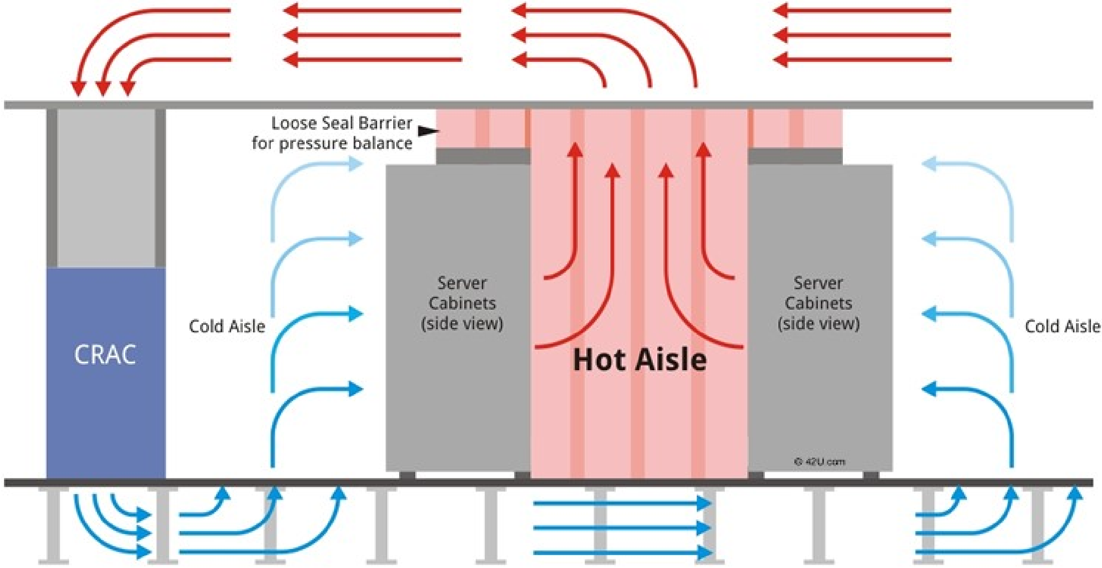

Figure 1-1: Air cooled data center [25]

1.3 Liquid Cooling of data servers:

To overcome the limitations of air cooling and free cooling, it is imperative to adopt a more efficient method of data center cooling. It is made more efficient by adopting liquid cooling method. Firstly, higher specific heat and thermal conductivity of liquids enhance augmented heat dissipation, keeping the junction temperature of the highly powered dense packages below the threshold limit [7]-[9]. Secondly, increased temperature of the coolant posits the possibility of energy reuse. For example, heat can be built from hot water in data centers in moderate climates. Also, reliability of operation of rack level data servers and electronic equipment in data centers is enhanced, with improved functionality [10]-[12]. Also, space consumed by axial fans are reduced, with lesser noise and smoother operation. Liquid cooling is performed by the following two methods:

1.4 Indirect liquid cooling

1.5 Direct liquid cooling

1.4 Indirect liquid cooling

In this method, water is used for liquid cooling, using a passive component called cold plate. The cold plate is placed on the processor and the heat is transferred to the copper base of the cold plate through conduction mode of heat transfer, increasing the temperature of the cold plate. The generated heat is directed to the water flowing inside the cold plate through convection. Chillers cool down the water, and it is recycled again. Due to high specific heat and thermal conductivity of water, rate of heat transfer is

drastically increased, as opposed to that of air cooling [13]. However, the servers cannot directly be submerged inside water, due to its non-dielectric feature. Fans are still required to cool the minor heat generating components. Also, tubes and ducting systems are required to direct the water flow, increasing the cost of experimental setup, with possibilities of leakage of water. To tackle these drawbacks, direct liquid cooling is a commonly adopted method that ensures efficient transfer of heat, eliminates leakage and simplifies the setup for the cooling operation [14]-[16].

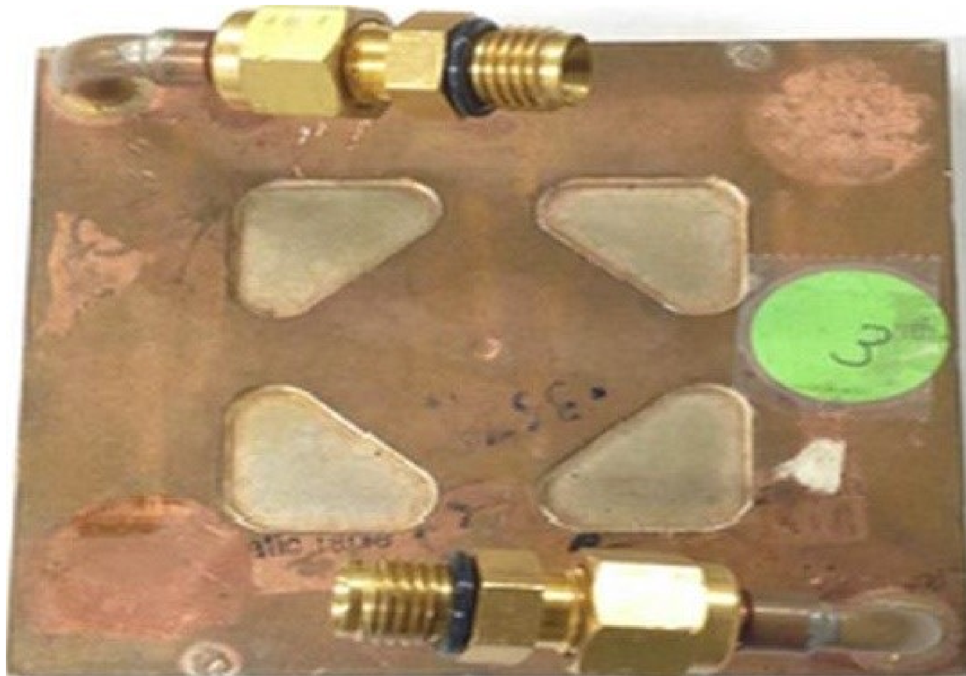

Figure 1-2: Cold Plate [25]

1.5 Direct liquid cooling

The dielectric feature of the liquid allows direct submersion of servers, and the heat generated by the server is carried away by the dielectric liquid. The flow rate of the fluid is regulated by the flow meter. Due to the high specific heat is to volume ratio of the fluid, being 1200-1400 times greater than air, constant server temperature is maintained, irrespective of the server workload, keeping the server in a uniform temperature environment, thus reducing the temperature gradients and fluctuations. Possibility of dust particles and contaminants entering the server is reduced, maintaining server hygiene. This is an added advantage. The accumulation of dust and contaminated particles inside the chassis of the computer leads to mechanical failure. With no moving parts like fans, cost of operation is also drastically reduced. Other benefits of immersion cooling are even temperature for the PCB, with prevention of oxidation or corrosion of electrical contacts and no sensitivity to any temperature condition [9], [17], [23], [25].

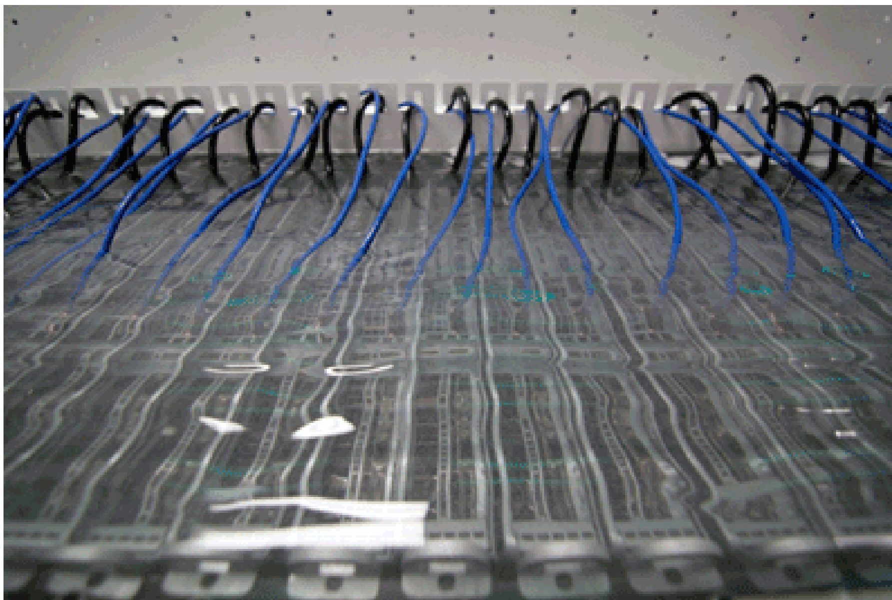

Figure 1-3: Dielectric cooled server [25]

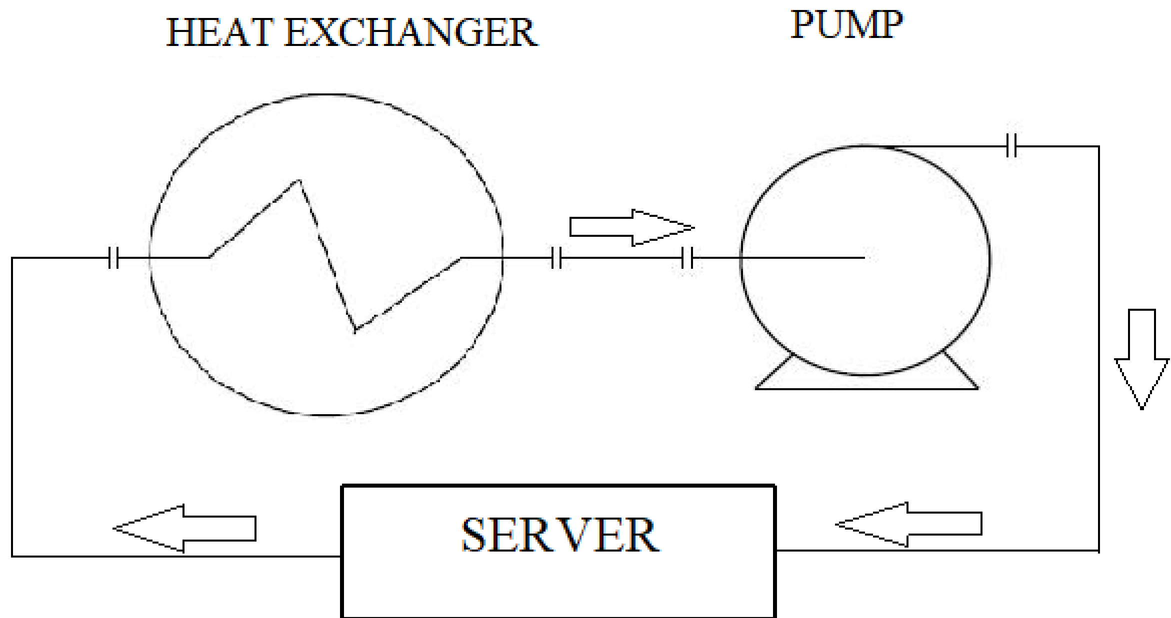

Figure 1-4: Schematic of an immersion cooled system [9]

The immersion cooling can be classified as:

i) Single-Phase Immersion Cooling

Figure 1-5 shows the process of Single-Phase Immersion Cooling. In this process, the coolant does not change its phase by boiling or freezing and remains in liquid phase. The heat exchanger receives the cold-water input from the water-cooling tower. The heat generated from the server gets transferred to the coolant at a lower temperature. The heated liquid gets pumped to the heat exchanger and gets cooled in the heat exchanger. The warm water output gets pumped to the water-cooling power from the heat exchanger, with the help of a water pump. The technique of open bath is used in the process, since there is little or no risk of coolant evaporation [25].

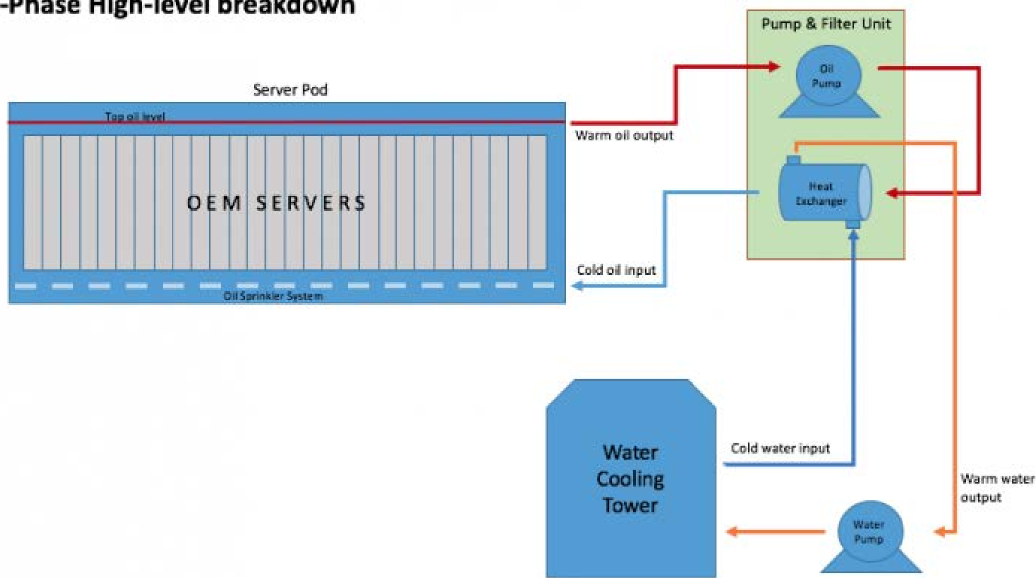

Figure 1-5: Single-Phase immersion cooling [25]

ii) Two-Phase Immersion Cooling

Figure 1-6 illustrates the process of Two-Phase Immersion Cooling, where the working fluid boils and exists in liquid and gas phase. It is viewed as a viable technology to meet the cooling needs of the high computing processors and dense packages in the market. The concept of latent heat, which is the thermal energy required to change the phase of the fluid is used. The temperature of the fluid is maintained at boiling point, since it is only cooled by boiling. The energy transferred from the heat source will cause a portion of the working fluid to boil off into a gas. The gas rises above the fluid pool contacts a condenser which is cooler than the saturation temperature, causing the fluid to condense back into a liquid and fall (rain) back into the pool. This immersion cooling method required semi-open baths, where the system is sealed to avoid the evaporation of coolant [25].

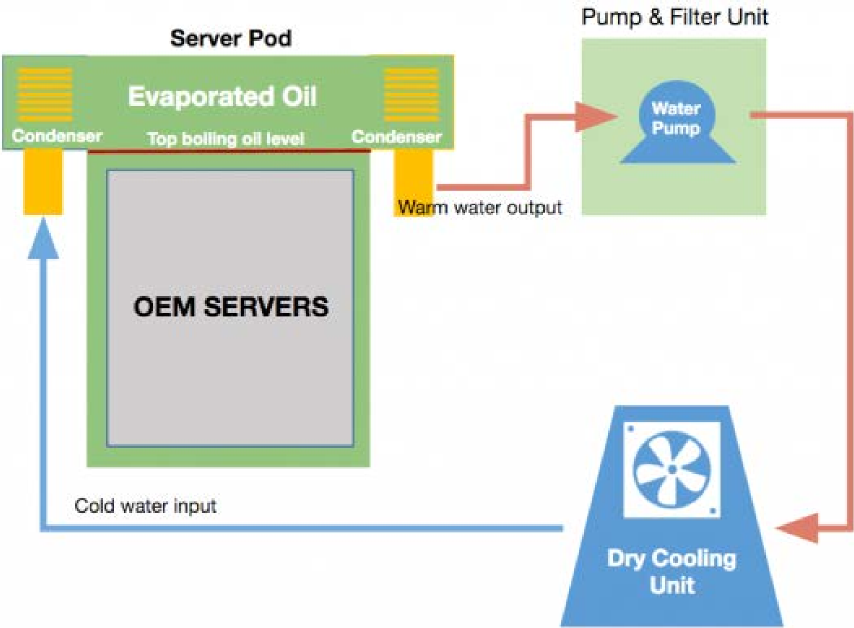

Figure 1-6: Two-Phase immersion cooling [25]

Chapter 2

MOTIVATION AND OBJECTIVE

Improvement in the immersion cooling method for better thermal performance and substantial energy savings are being tested by using nanofluids, with the size of the nanoparticles of 1 to 150 nanometres. Due to the poor thermal conductivities of traditional heat transfer fluids such as water, oil, and ethylene glycol mixture, adding nanoparticles in appropriate concentrations increases the thermal conductivity of the fluid. Metals in solid form exhibit larger thermal conductivity than fluid by orders of magnitude. For example, the thermal conductivity of copper is 3000 times greater than the thermal conductivity of water at room temperature. To keep the dielectric feature of the liquid, oxides of metal such as Al2O3, having larger magnitudes of thermal conductivities compared to water, can be added to base fluids for immersion cooling. Superior heat transfer properties are expected to be exhibited by nanofluids compared to the conventional base fluids. Since heat transfer occurs at the surface, it is desirable to use particles with a large surface area. The large surface area of nanoparticles should improve the heat transfer capabilities, with enhancement in the stability of the suspension [24].

Rea et al. [26] reported enhancement in the heat transfer coefficient at 6 vol% alumina nanofluid compared to water in the entrance region, with a lower enhancement displayed by zirconia nanofluid. Numerical and experimental analysis of laminar convective heat transfer of TiO2/Water Nanofluid flowing through a uniformly heated circular tube was conducted by Ebrahimnia-Bajestan et al. [27], reporting a maximum increase of 21% in

the average heat transfer coefficient at 2.3 vol% of TiO_2. Ghale et al. [28] performed a CFD analysis of Al_2O_3/water nanofluid in a straight and ribbed MHCS resulting in a 16.1% increase in Nu from 1% to 2% in the volume fraction of alumina. Duangthongsuk et al. [29] Observed higher heat transfer coefficient values with the use of TiO_2/water as compared to base fluids, with Pak and Cho's correlation agreeing better with the results of experimentation. Hwang et al. [30] Conducted experimentation which showed the good agreement of Darcy friction factor with theoretical results of the friction factor correlation for the single-phase flow (64ReD). Also, an 8% increase in the heat transfer coefficient was reported for Al_2O_3/Water nanofluid at 0.3% under the fixed Re as compared to that of pure water. Jung et al. [31] measured the friction coefficient of Al_2O_3 nanofluid of 170 mm diameter, observing the increase in heat transfer coefficient of nanofluids with the base fluid of water and ethylene glycol at a volume fraction of 1.8 volume percent without major friction losses. From the study on nucleate pool boiling heat transfer of TiO_2-R141b nanofluids by Trisaksri et al. [32], no significant effect on the nucleate boiling heat transfer of R141b was observed.

About the literature survey on the liquid cooling using nanofluids, results on the numerical analysis of oil immersion cooling using Al_2O_3 and Mineral Oil on a Winterfell server is documented in the study. The server and its components are modeled using Ansys Icepack. With the help of available theoretical data and equations, mechanical properties of the nanofluid are calculated. The chosen mass concentrations of Al_2O_3 are 0%, 1%, 3%, and 5%, and its effects on the temperature reduction of the server and its components are tested. Simulations are performed for 3 different heatsink configurations at different

inlet temperatures of 25, 35, and 45 °C with volumetric flow rates of 0.5, 1, 2 and 3 LPM to determine the best case to be used for experimental analysis.

Chapter 3

GEOMETRY, METHODS AND FORMULA

3.1 Server Description

The server used in the current study is the Third Generation Open Compute Server. It consists of two CPUs with a TDP of 65 W each and the heatsinks are mounted on them respectively. The cabinet houses 16 RAM units on either side of the heatsinks with 4 GB memory each. The server has dimensions of (700mm ×170mm×87mm). The two fans that were originally present for air cooling are removed from the current model. The baseline model of the server is designed using ANSYS Icepak as shown in figure 3-1.

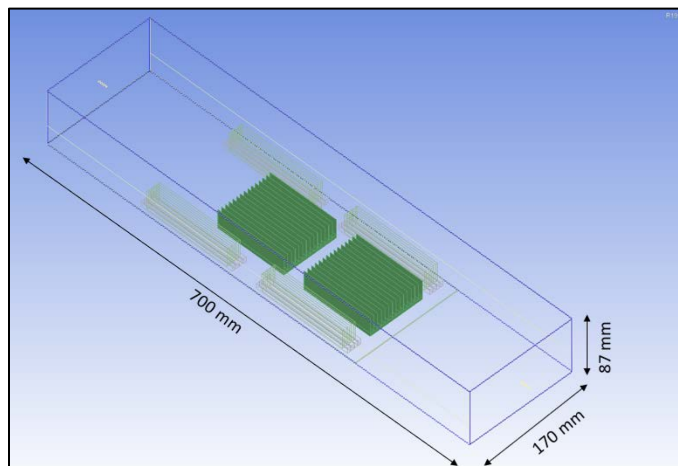

Figure 3-1: Baseline model of the immersion cooled server

Figure 3-2: The 3rd generation open commute server used in the current study [25]

3.2 Boundary Conditions

The model incorporates an inlet and outlet in the x-direction. At the inlet of the cabinet, the flow velocity is specified based on the volumetric flow rate, with inlet temperatures varied. Velocities in the y and z directions are assumed to be zero. The outlet is maintained at ambient pressure. Periodic boundary conditions are applied in the z-direction to account for repetitive servers in an experimental setup. The top and bottom walls in the y-direction are maintained at a constant heat flux of $0 W/m^2$. The surroundings have a temperature of 30 ℃ with a pressure of 1 atm. The boundary conditions are summarized as follows:

Inlet:

u_x = 0.00163, 0.00326, 0.00652 and 0.00978 m/s

$u_y = u_z = 0$

Temperature: 25, 35 and 45 ℃

Outlet:

Static Pressure = Ambient (1 atm)

Wall type: Stationary

Heat Flux: 0 W/m^2

And the rest assumed as periodic boundaries

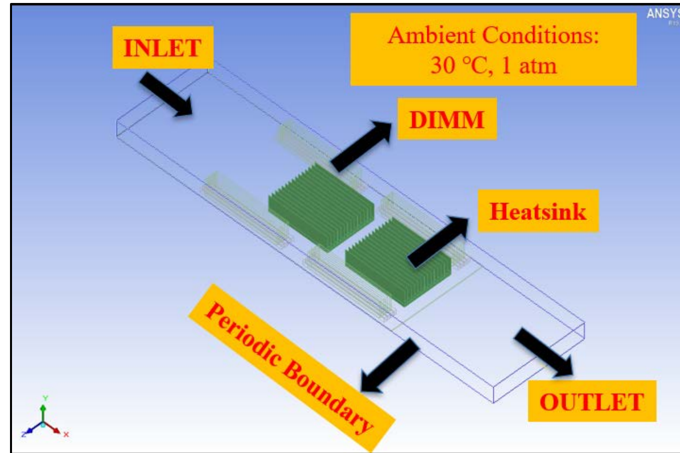

Figure 3-3: Boundary conditions for the baseline model

3.3 Properties of the Nanofluid

The properties of nanofluid are calculated by the following equations, based on the temperature-dependent properties of pure mineral oil and physical properties of AL2O3, as shown in Table 1 and 2 [33]:

Density: $\rho_{nf} = (1 - \emptyset)\rho_f + \emptyset\rho_s$ (1)

Where $\emptyset$ is the mass concentration of Al2O3 is, ρ_s is the density of Al2O3, ρ_f is the density of pure mineral oil and ρ_{nf} is the density of the nanofluid.

Specific Heat Capacity: $C_{P_{nf}} = \frac{(1-\emptyset)(\rho C_p)_f + \emptyset(\rho C_p)_s}{\rho_{nf}}$ (2)

Where C_{pf} is the specific heat of pure mineral oil, and $C_{P_{nf}}$ is the specific heat of the nanofluid.

Viscosity: $\mu_{nf} = \mu_f(1 - \emptyset)^{-2.5}$ (3)

Where μ_f is the viscosity of pure mineral oil and μ_{nf} is the viscosity of the nanofluid.

Thermal Conductivity: $K_{nf} = K_f\left[\frac{K_s+2K_f-2\emptyset(K_f-K_s)}{K_s+2K_f+\emptyset(K_f-K_s)}\right]$ (4)

Where K_s is the thermal conductivity of Al2O3, K_f is the thermal conductivity of pure mineral oil, and K_{nf} is the thermal conductivity of the nanofluid.

Thermal Expansion Ratio: $\beta_{T_{nf}} = \frac{(1-\emptyset)(\rho\beta_T)_f+\emptyset(\rho\beta_T)_s}{\rho_{nf}}$ (5)

Where β_{Ts} is the thermal expansion ratio of Al2O3, β_{Ts} is the thermal expansion ratio of Al2O3 and $\beta_{T_{nf}}$ is the thermal expansion ratio of the nanofluid.

Table 1**:** Properties of pure mineral oil

Temperature °C	ρ_f Kg/m3	C_{pf} J/Kg-K	μ_f Kg/m-s	K_f W/m-k	β_{Tf}
25	867	1940.04	0.0197	0.133	0.00075
40	857	1990.25	0.01119	0.13	0.00076
60	845	2064.78	0.006355	0.128	0.00078
80	832	2140.68	0.004111	0.126	0.0008

Table 2: Physical properties of AL2O3 [34]

Physical Properties	Al2O3
C_p (W/m-k)	765
ρ (Kg/m^3)	3970
K (W/m-k)	40
$\alpha \times 10^7$ (m^2/s)	131.7
β $(K^{-1} \times 10^{-6})$	8.5

3.4 Thermal Conductivity and Specific Heat

From equations 2 and 4, thermal conductivity and specific heat at various concentrations of Al2O3 are calculated. The physical properties of Al2O3 are shown in Table 2.

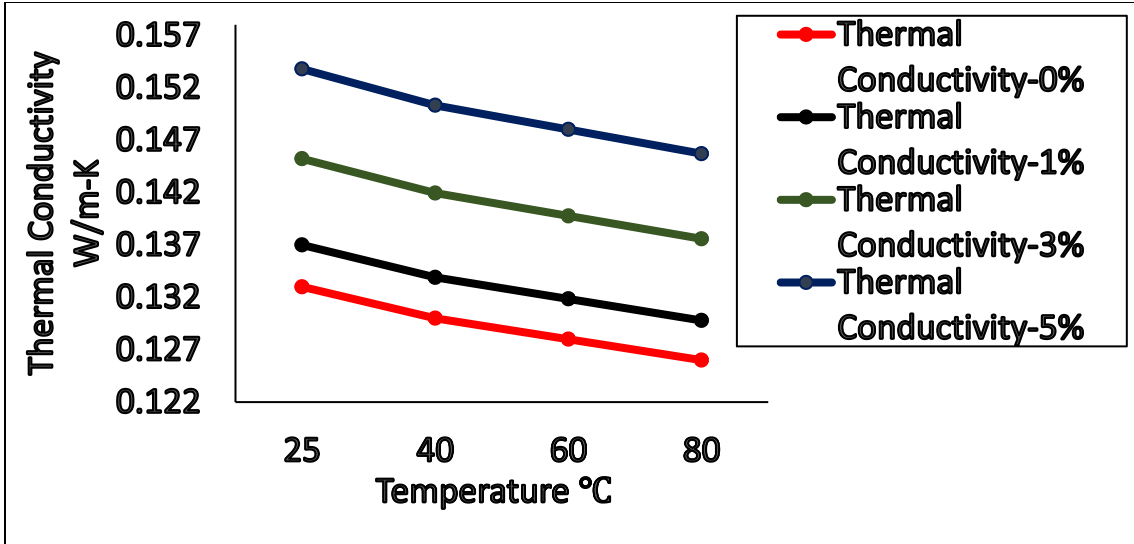

Figure 3-4: Variation of thermal conductivity with temperature at 0 and 5 mass% of Al2O3

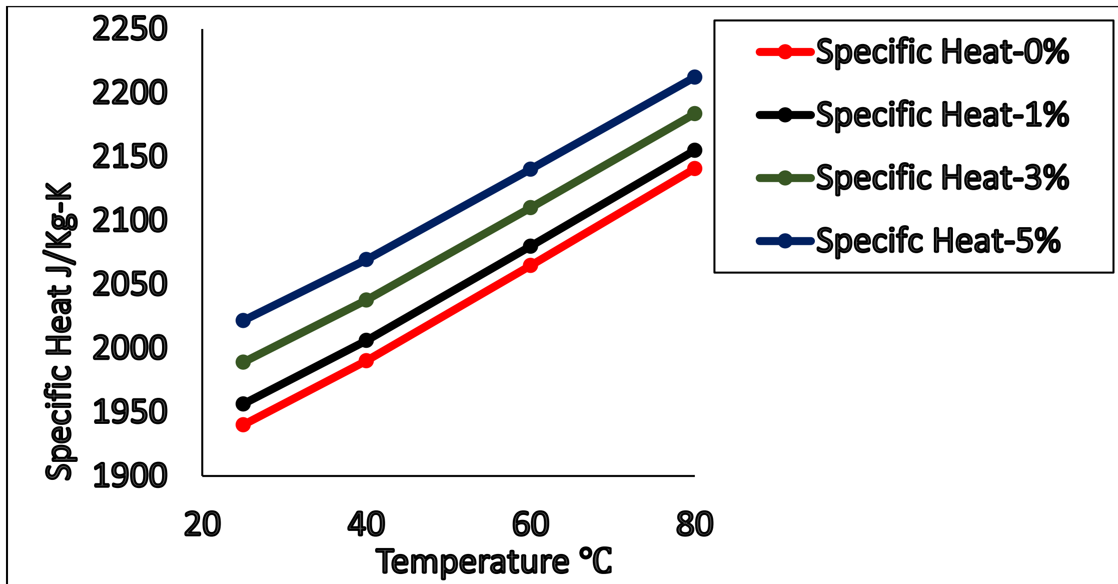

Figure 3-5: Variation of specific heat with temperature at 0 and 5 mass% of Al2O3

Graphs are plotted to study the trends in thermal conductivity and specific heat with nanoparticle mass% concentration and temperature. Figures 3-4 and 3-5 show the variation of thermal conductivity and specific heat with temperature, at 0, 1, 3, and 5 mass% of Al2O3 nanoparticles. The maximum increase in thermal conductivity is observed at 5 mass% concentration of Al2O3 and inlet temperature of 25 ℃, from an increase of 0.133 to 0.153 W/mK. A decrease in thermal conductivity with temperature is due to the increase in the randomness of molecular movements, obstructing the flow of heat through the liquid. The molecular diffusion effect is more pronounced at higher temperatures, manifested in the decrease of thermal conductivity from 0.153 to 0.145 W/mK at 5 mass% concentration, between 25 and 45 ℃ inlet temperature.

Also, an increase in nanoparticle concentration from 0 to 5 mass% results in the rise of specific heat, with a maximum enhancement of $C_p = 82\ J/KgK$ observed at 25 ℃ inlet temperature. At higher temperatures, an increase in specific heat is due to the increase in the average temperature of the nanoparticles, with lesser enhancement in the specific heat between 0 and 5 mass% Al2O3 concentration. Thermal conductivity and specific heat of the fluid at 40 ℃ at different concentrations are shown in table 3.

Table 3**:** Thermal conductivity and specific heat 40 ℃

Thermal Conductivity (W/m-K)	Specific Heat (J/Kg-K)	Concentration (%)
0.13	1990.25	0
0.133901	2006.08	1
0.141941	2037.73	3
0.150317	2069.39	5

3.5 Governing Equations

The flow is assumed to be laminar due to Re<<<230. Ansys Icepak solves the Navier-Stokes equation on the conservation of mass, momentum, and energy, with the specified parameters and boundary conditions. The governing equations solved for simulations are as follows:

$$\frac{\partial \rho}{\partial t} + \nabla.(\rho \vec{v}) = 0 \quad (6)$$

For an incompressible flow, equation (6) reduces to:

$$\nabla.\vec{v} = 0 \quad (7)$$

$$\frac{\partial(\rho \vec{v})}{\partial t} + \nabla.(\rho \vec{v}\vec{v}) = -\nabla p + \nabla.(\bar{\bar{\tau}}) + \rho \vec{g} + \vec{F} \quad (8)$$

Where p is the static pressure, $\bar{\bar{\tau}}$ is the stress tensor, and $\rho \vec{g}$ is the gravitational body force. $\vec{F}$ May arise from resistances, sources and so on ([32]).

$$\frac{\partial(\rho h)}{\partial t} + \nabla.(\rho h \vec{v}) = -\nabla.[(k + k_t)\nabla T + S_h \quad (9)$$

Where k is the molecular conductivity, k_t is the conductivity due to turbulent transport and S_h includes the defined volumetric sources

3.6 Heatsinks

Heatsinks are passive components that are thermally conductive, which carries away heat from the CPU into the fins that provide a large surface area for the dissipation of heat throughout the rest of the computer, keeping the temperature of the processor and the heatsink low. The fins present in the heatsink increase the surface area for the enhanced heat transfer between the heat producing components and the cooling medium. Efficiency of heatsinks are increased with the use of heat spreaders between the heat source and secondary heat exchanger that transfers heat uniformly with a more favorable surface area and geometry than the source. A highly thermally conductive material is used for the design of heat spreaders to ensure maximum transfer of heat. Copper or Aluminum alloys are the commonly used materials for manufacturing heat spreaders due to their favorable heat transfer characteristics, and high thermal conductivity, that leads to enhanced thermal performance. The types of heatsinks used in the study were Parallel Plate, Pin Fin and Plate Fin Heatsinks. The baseline model of the parallel plate heatsink is shown in figure 3-6.

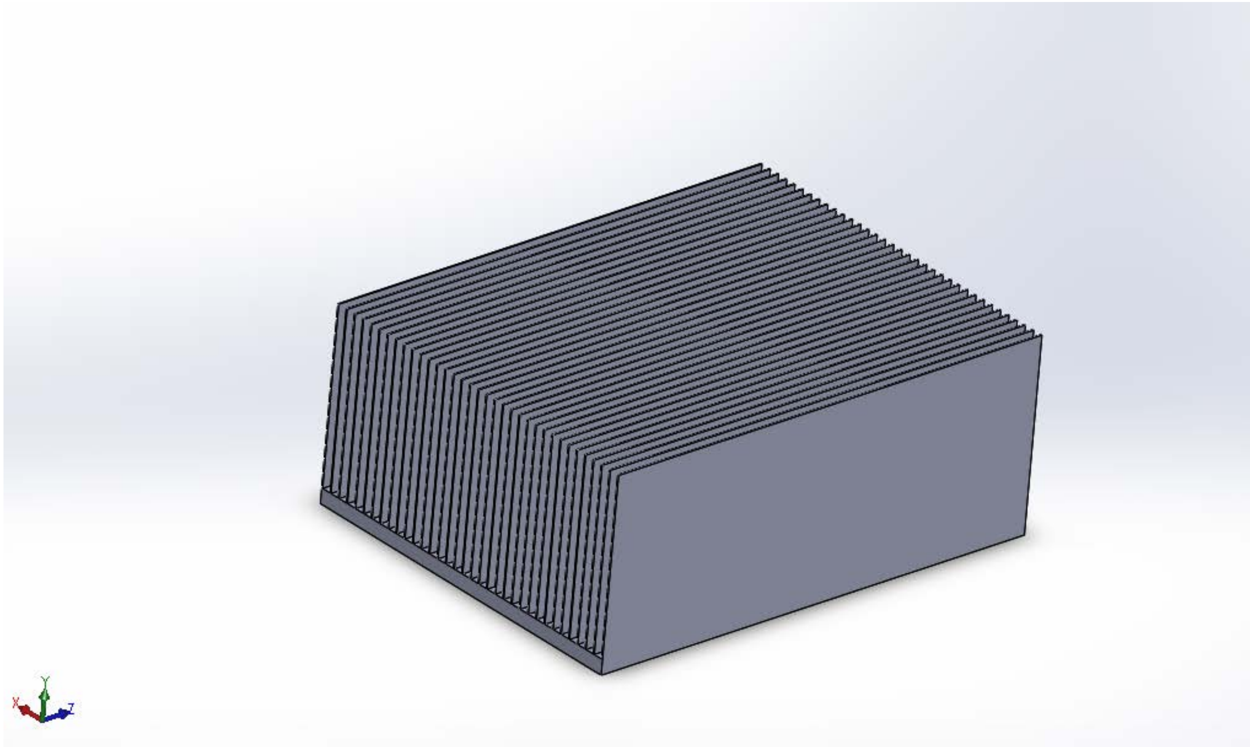

Figure 3-6: Baseline model of the parallel plate heatsink [25]

3.7 Optimization of Heatsinks:

Table 4: Dimensions of the baseline model of the parallel plate heatsink [25]

Thickness	0.3
Height	41
Length	110
No of fins	35

All dimensions are in mm

Table 4 shows the dimensions of the baseline model of the parallel plate heatsink. Optimization of the heatsink is performed to determine the geometry of the heatsink

based on the required thermal performance and application. In the current study, Ansys Icepak was used as a mathematical tool for the optimization of the parallel plate heatsink, to enhance the reduction in the maximum CPU junction temperature. Table 5 shows the dimension of the parallel plate heatsink after optimization.

Table 5**:** Dimensions of the optimized model of the parallel plate heatsink

Thickness	0.25
Height	30
Length	110
Number of fins	15

All dimensions are in mm

To test the effect of heatsink geometry on the reduction of the maximum CPU junction temperature, pin fin and plate fin heatsink geometries were modelled in Ansys Icepak. The detailed modelling and description of the heatsink geometries are shown in the figures and tables below.

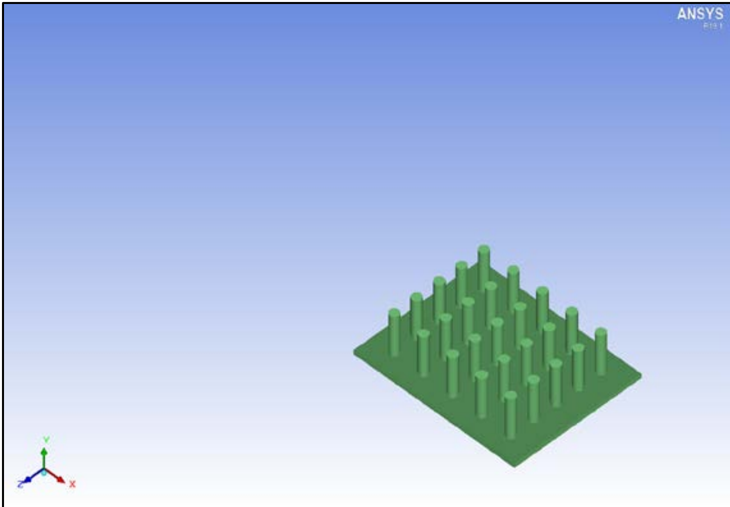

Figure 3-7: Optimized model of the pin fin heatsink [25]

Table 6: Dimensions of the Pin Fin Heatsink [25]

Pin Radius	3
Height	30
Length	110
No of fins (x)	5
No of fins (z)	5
Offset (x)	5
Offset (z)	5
Pin Alignment	Inline

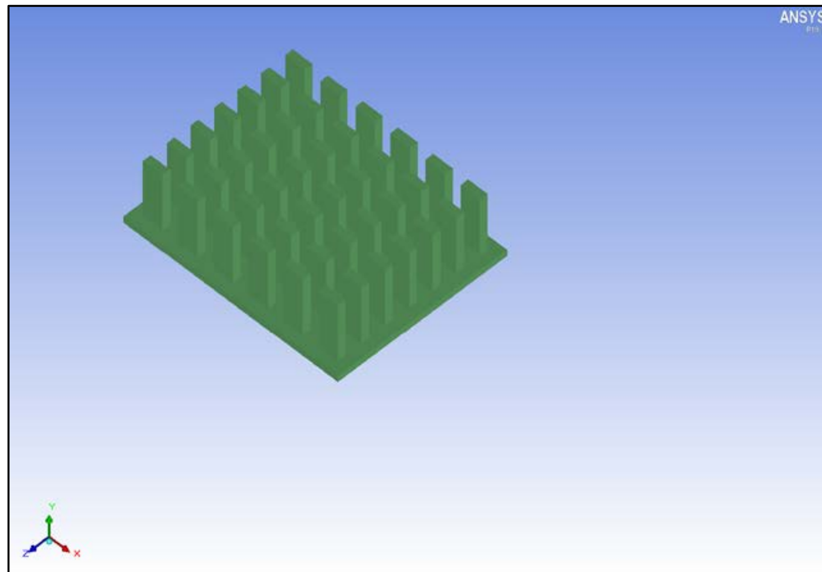

Figure 3-8: Optimized model of the plate fin heatsink [25]

Table 7**:** Dimensions of the plate fin heatsink [25]

Height	30
Length	110
No of fins (x)	6
No of fins (z)	7
Offset (x)	5
Offset (z)	5
Thickness (x)	10
Thickness (z)	4

3.8 Mesh Sensitivity Analysis

From the graph shown on the maximum CPU temperature v/s the maximum no of elements in the model in Figure 3-5, the maximum CPU temperature remained nearly constant after an element count of around 1.1 million. For the rest of the study, no of Elements was in the range of 1.1 to 1.9 million elements. The graph was obtained for a flow rate of 0.5 LPM of pure mineral oil.

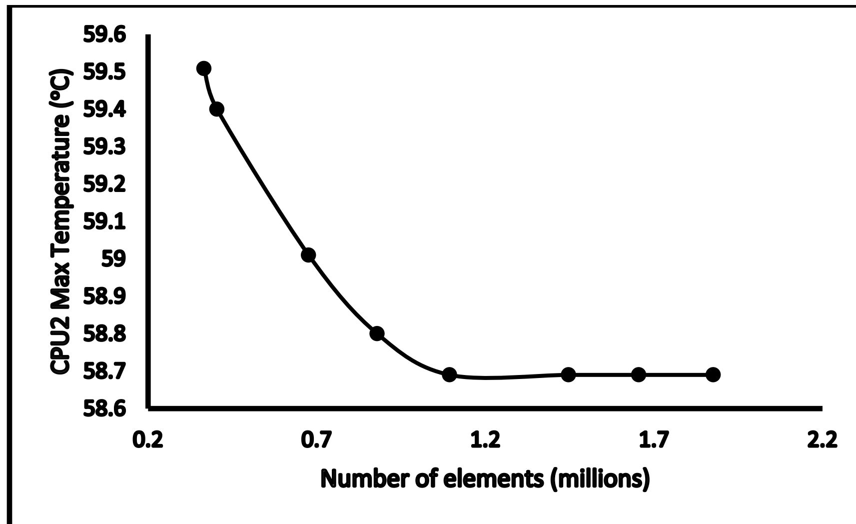

Figure 3-9: Mesh Sensitivity Analysis

3.9 Effect of cabinet height on CPU temperature:

Before the study, two simulations were conducted using pure mineral oil at 0.5 LPM to test the effect of cabinet height on CPU temperature. Heights of 87 mm and 30 mm were chosen and a 34% reduction in maximum CPU junction temperature was observed after stimulation, as shown in figures 3-10 and 3-11.

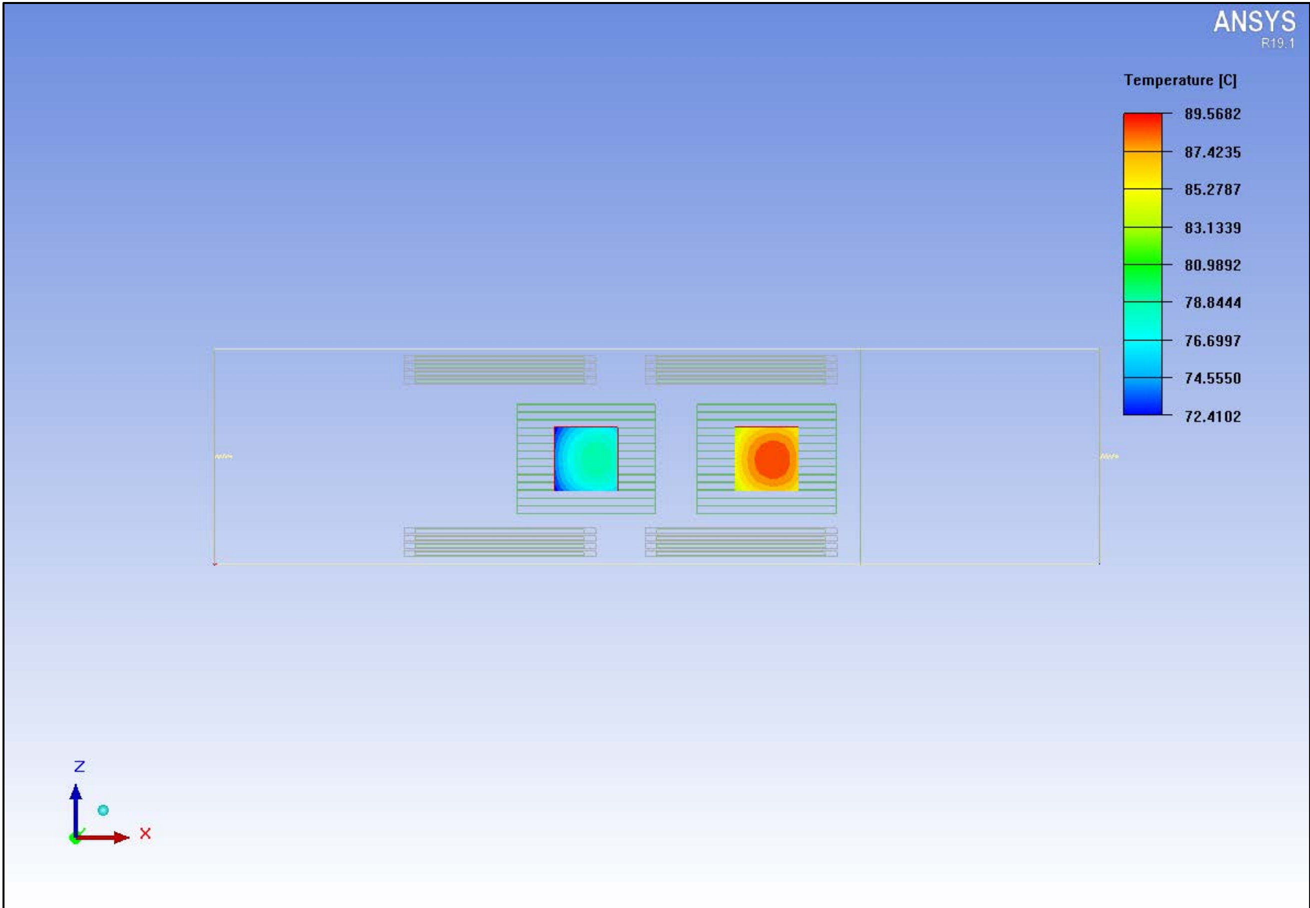

Figure 3-10: CPU temperature with standard frame height

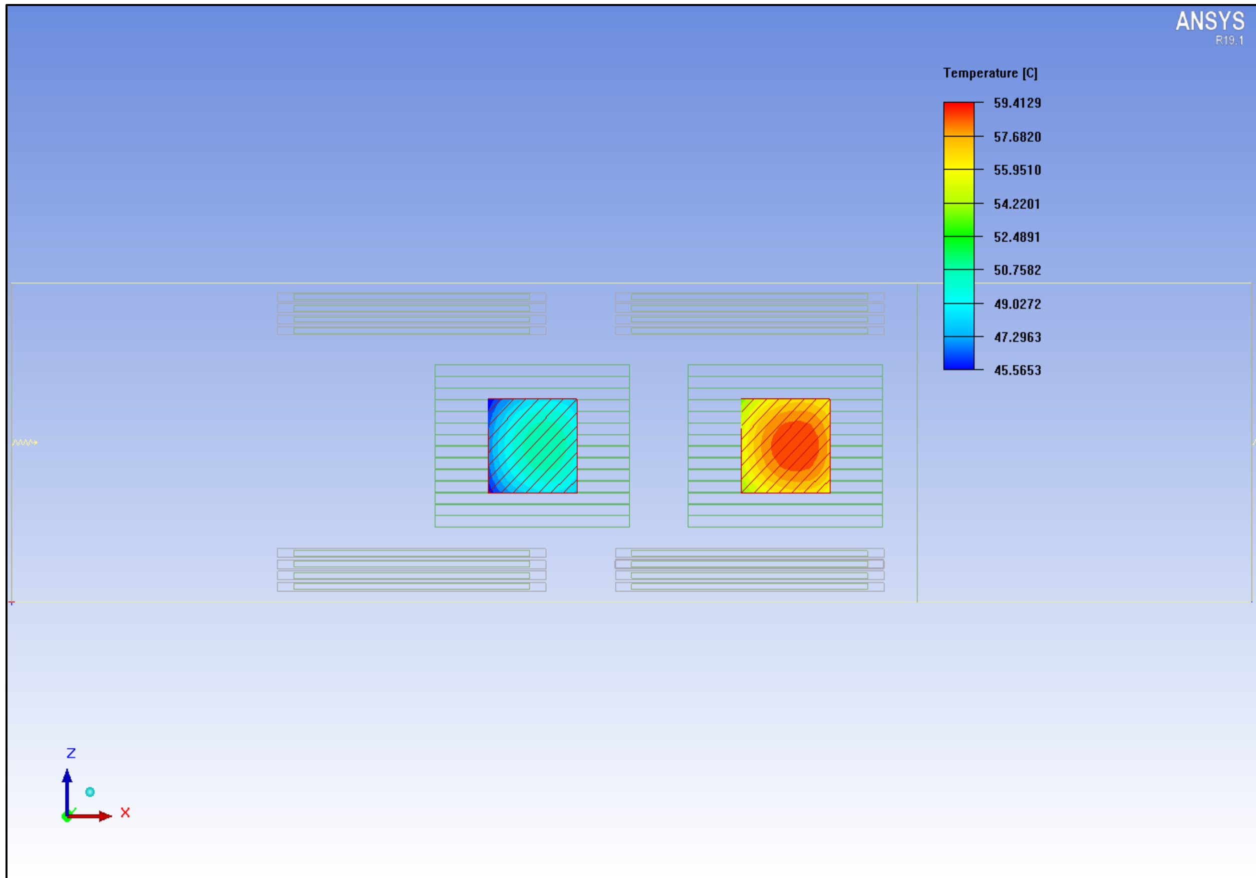

Figure 3-11: CPU temperature with reduced frame height

The fluid tends to follow a path of least resistance. A larger frame height offers least resistance above the heatsinks for the fluid flow. On the contrary, smaller frame height regulates the fluid to flow through the heatsinks, enhancing the reduction in CPU temperatures. The cabinet height is maintained at 30 mm for the rest of the study. The velocity contours for the two simulations are displayed in Figures 3-12 and 3-13 respectively.

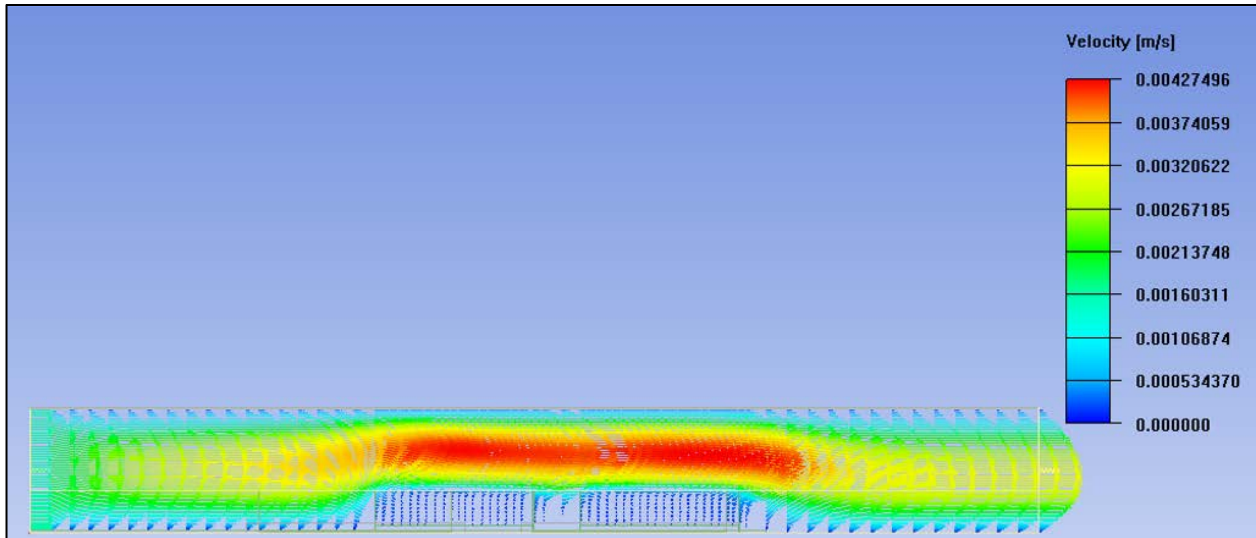

Figure 3-12: Velocity profile with standard frame height

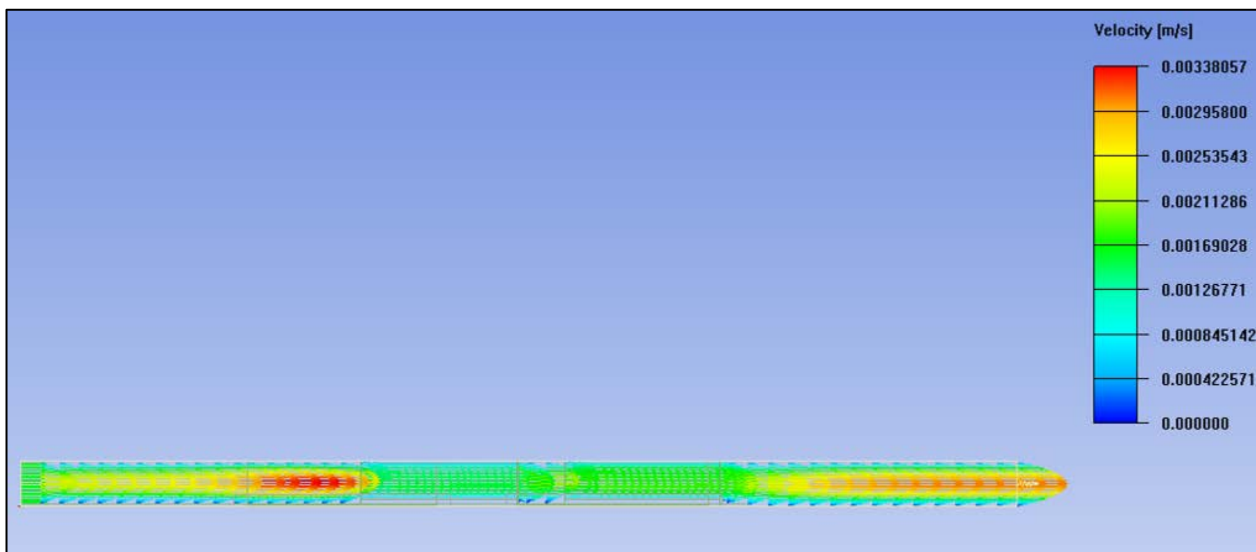

Figure 3-13: Velocity profile with reduced frame height

Chapter 4

RESULTS AND DISCUSSION

4.1 Effect of nanoparticle concentration and flow rate on the maximum CPU junction temperature and pressure drop for the parallel plate heatsink configuration:

Simulations were performed for flow rates of 1, 2 and 3 LPM for the Al2O3 mass concentration of 0, 1, 3 and 5% respectively, to test their effects on the maximum CPU junction temperature, pressure drop and pumping power for the three heatsink configurations.

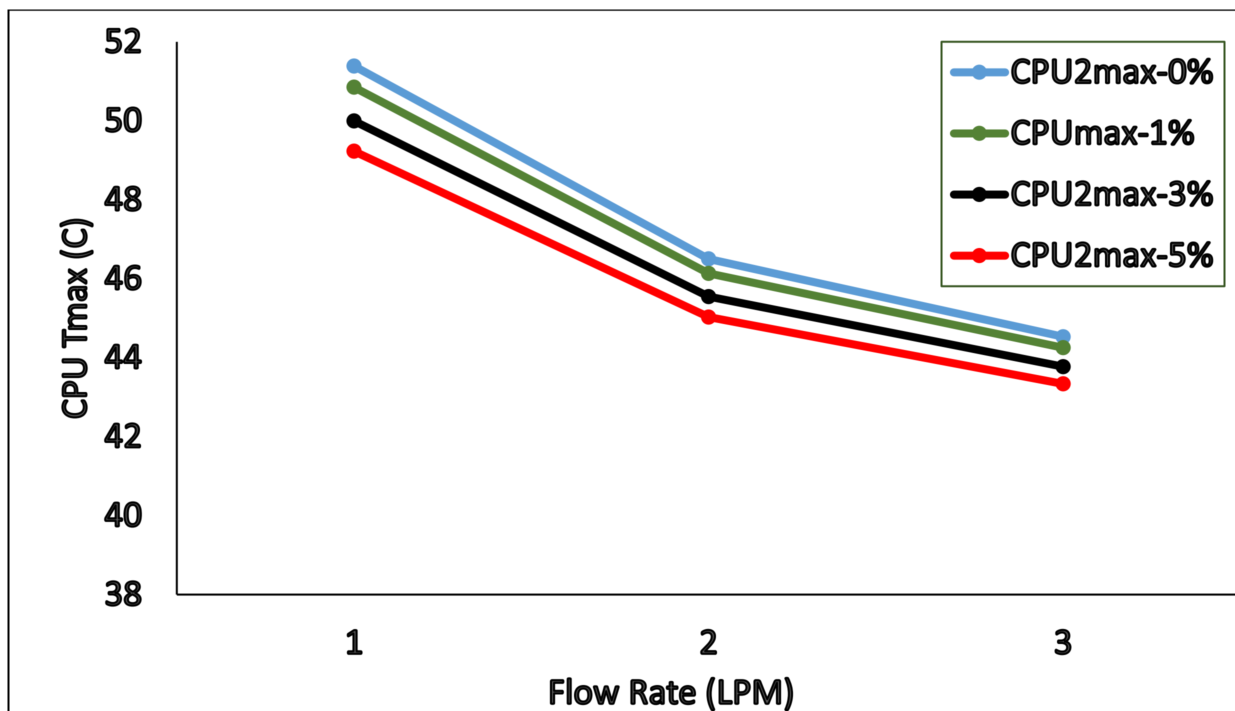

Figure 4-1: Variation of CPU Tmax with flow rate at different mass% of Al2O3 for parallel plate heatsink geometry

Figure 4-1 shows the variation of maximum CPU temperature with flow rates of 1, 2 and 3 LPM, for 0, 1, 3 and 5 mass% of Al2O3 for the parallel plate heatsink geometry. The maximum CPU temperature decreases exponentially with flow rate, from a temperature of 51.38 °C to 44.53 °C for 0% concentration of Al2O3. The above trends also highlight the reduction in CPU Tmax with the increase in nanoparticle concentration from 0 to 5 mass % of Al2O3 in pure mineral oil. At 1 LPM flow rate, maximum reduction of 2.16 °C is obtained, by increasing the mass% of Al2O3 from 0 to 5%. By increasing the nanoparticle concentration to 5% and flow rate to 3 LPM, a maximum reduction of 8 °C can be obtained. Larger flow rates can reduce CPU Tmax, but also increases pressure drop significantly. Hence, the effect of flow rate and nanoparticle concentration on the pressure drop is explained in figure 4-2.

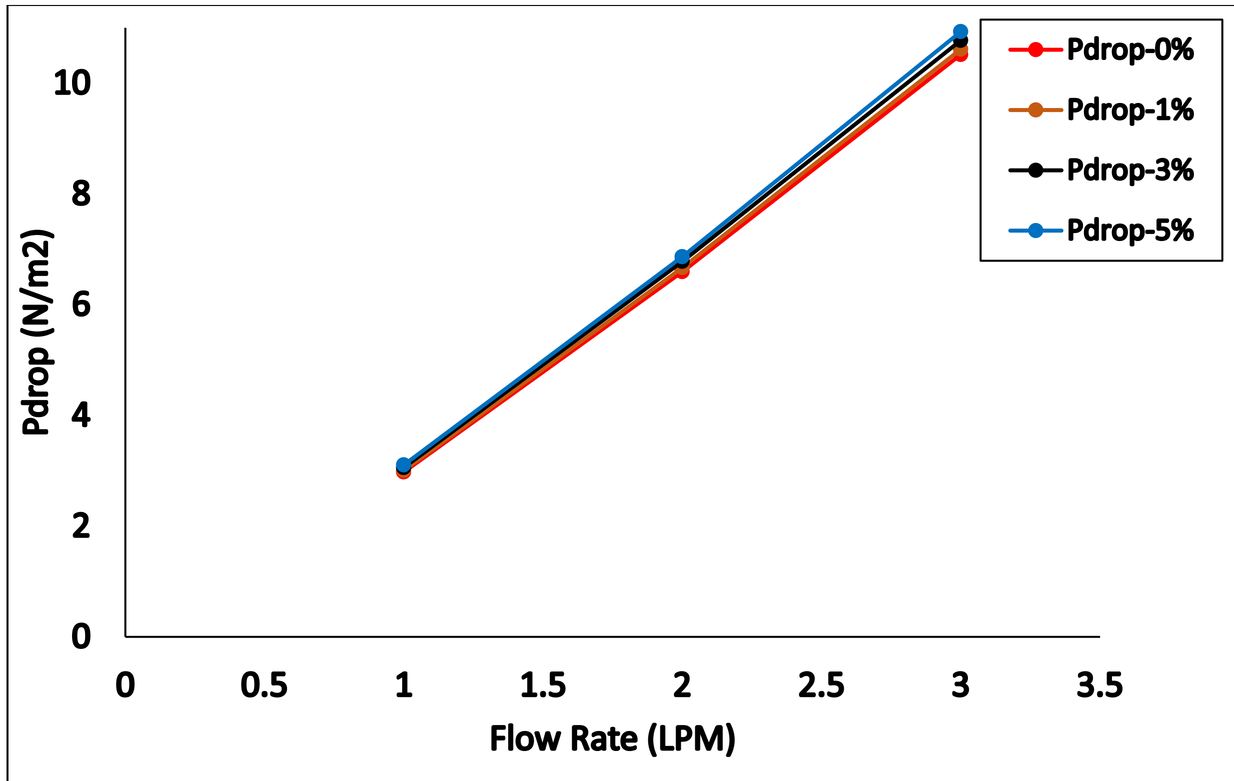

Figure 4-2: Variation of Pdrop with flow rate at different mass% of Al2O3 for parallel plate heatsink geometry

Figure 4-2 shows the variation of pressure drop with flow rates of 1, 2 and 3 LPM, for 0, 1, 3 and 5 mass% of Al2O3 for the parallel plate heatsink geometry. The pressure drop increases exponentially with flow rate, from a value of 3.10 N/m2 to 10.92 N/m2 for 5 mass% concentration of Al2O3. At 0 mass% concentration of Al2O3, the pressure drop increases from 2.97 N/m2 at 1 LPM, to 10.51 N/m2 at 3 LPM flow rate. It can be inferred that exceeding the flow rate beyond 1 LPM can cause a significant increase in the pumping power, due to massive surge in pressure drop. However, increasing nanoparticle concentration from 0 to 5% does not cause a significant rise in the pressure drop, as

shown in the graphs. Maximum increase in pressure drop of only 0.33 N/m2 is obtained at 3 LPM. Hence a flow rate of 1 LPM at 5 mass% concentration is the most ideal case for the parallel plate heatsink geometry.

4.2 Effect of nanoparticle concentration and flow rate on the maximum CPU junction temperature and pressure drop for the pin fin heatsink configuration:

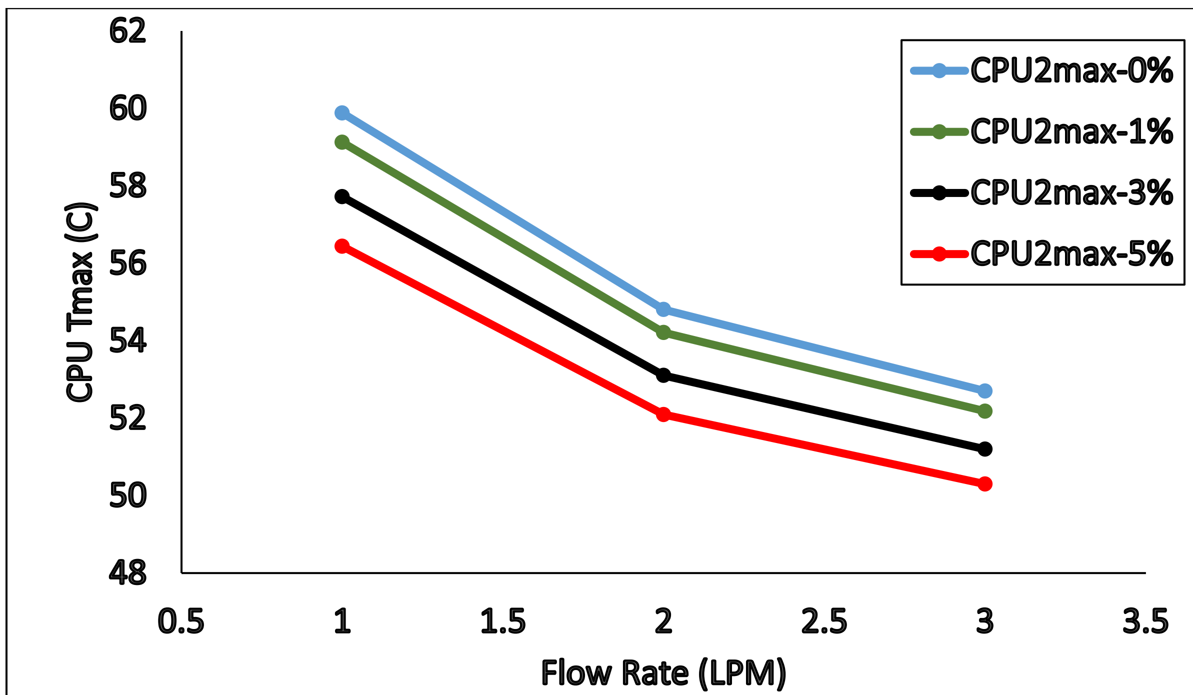

Figure 4-3: Variation of CPU Tmax with flow rate at different mass% of Al2O3 for pin fin heatsink geometry

Figure 4-3 shows the variation of maximum CPU temperature with flow rates of 1, 2 and 3 LPM, for 0, 1, 3 and 5 mass% of Al2O3 for the pin fin heatsink geometry. The maximum CPU temperature decreases exponentially with flow rate, with a maximum reduction in the CPU Tmax of 3.45 °C from 0 to 5 mass% of Al2O3, at 1 LPM flow rate. A higher reduction in the maximum CPU temperature is obtained as opposed to the parallel plate

heatsink geometry. This reduction in CPU Tmax is further enhanced by increasing the flow rate from 1 to 3 LPM, in increments of 1 LPM. A maximum reduction of 9.5 °C can be obtained by increasing the flow rate from 1 to 3 LPM, as opposed to an 8 °C drop, using the parallel plate heatsink geometry.

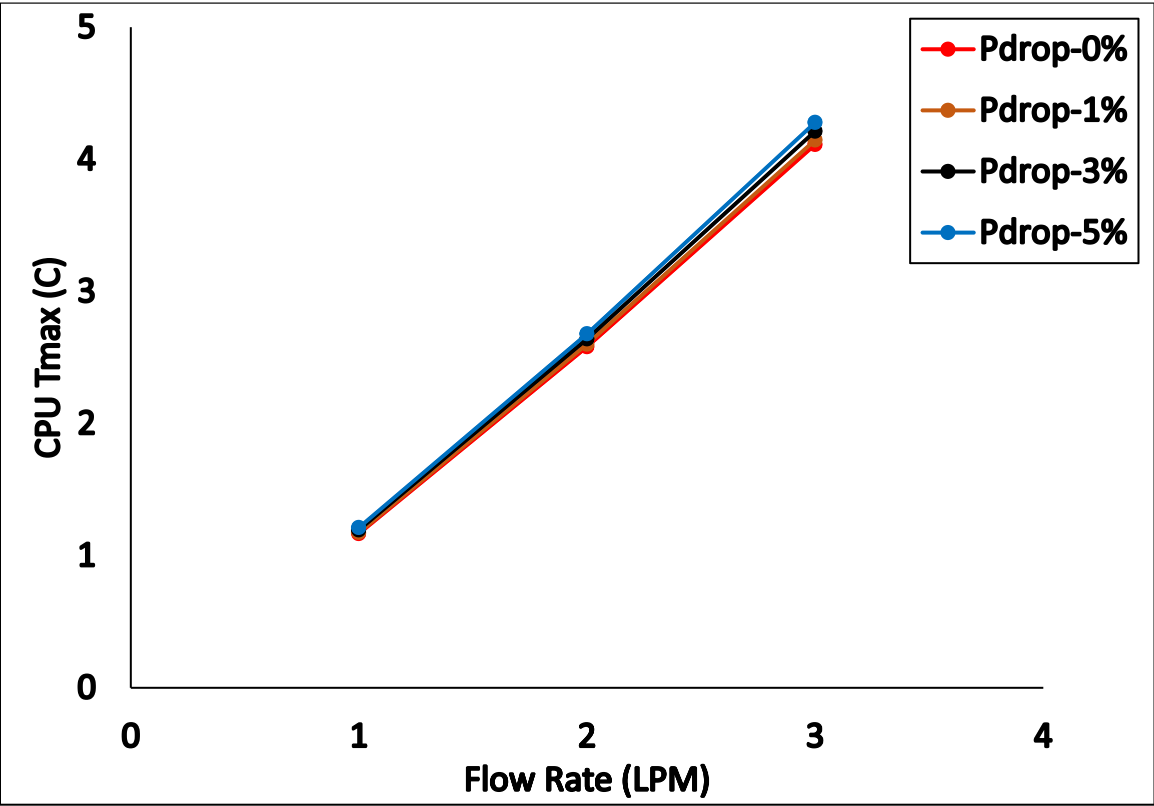

Figure 4-4: Variation of Pdrop with flow rate at different mass% of Al2O3 for pin fin heatsink geometry

Figure 4-4 shows the variation of pressure drop with flow rates of 1, 2 and 3 LPM, for 0, 1, 3 and 5 mass% of Al2O3 for the pin fin heatsink configuration. The pressure drop

increases exponentially with flow rate, from a maximum value of 1.21 N/m2 to 4.27 N/m2 for 5 mass% concentration of Al2O3. At 0 mass% concentration of Al2O3, the pressure drop increases from 1.16 N/m2 at 1 LPM, to 4.11 N/m2 at 3 LPM flow rate. The change in pressure drop at 5 mass% of Al2O3 is only 3.06 N/m2, as opposed to a 7.82 N/m2 increment in pressure drop, for the parallel plate heatsink geometry. At a flow rate of 2 LPM and 5 mass% of Al2O3, the pressure drop is approximately 61% lesser than the pressure drop obtained from the parallel plate heatsink geometry. However, negligible change in pressure drop of 0.04 N/m2 is obtained at a flow rate of 1 LPM. Hence, a flow rate of 1 LPM and 5 mass% Al2O3 is the best suited for the pin fin heatsink configuration.

4.3 Effect of nanoparticle concentration and flow rate on the maximum CPU junction temperature and pressure drop for the plate fin heatsink configuration:

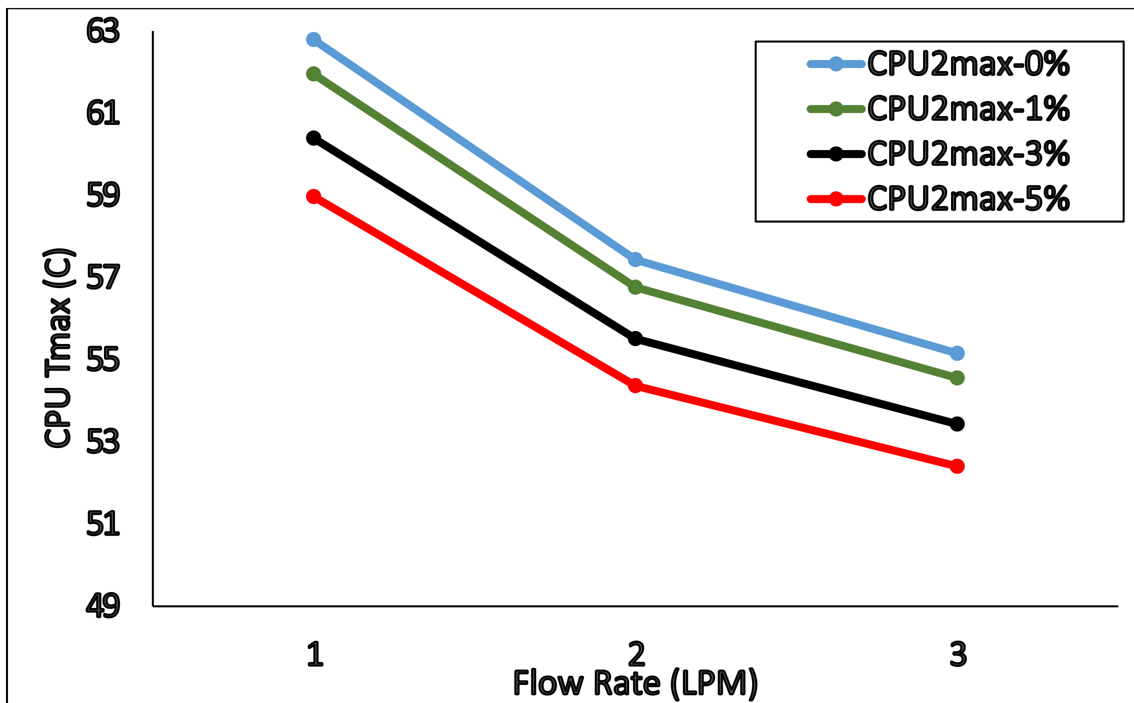

Figure 4-5: Variation of CPU Tmax with flow rate at different mass% of Al2O3 for plate fin heatsink geometry

The variation of maximum CPU temperature with flow rates of 1, 2 and 3 LPM, for 0, 1, 3 and 5 mass% of Al_2O_3 for the plate fin heatsink geometry, is shown in figure 4-5. The maximum CPU temperature decreases exponentially with flow rate, from a temperature of 62.78 °C to 55.15 °C for 0 mass% of Al_2O_3. The above trends shows the maximum reduction in CPU Tmax with the increase in nanoparticle concentration from 0 to 5 mass % of Al_2O_3 in pure mineral oil, of 3.87 °C. However, the CPU Tmax for the plate fin heatsink configuration is higher than that of the parallel plate and pin fin heatsink configurations. At 3 LPM and 5 mass% of Al_2O_3, the CPU Tmax is 52.40 °C, as opposed to a CPU Tmax of 50.29 °C for the pin fin heatsink geometry, and 43.33 °C for the parallel plate heatsink geometry. Effects of higher flow rate and nanoparticle concentration on the pressure drop is shown in figure 4-6.

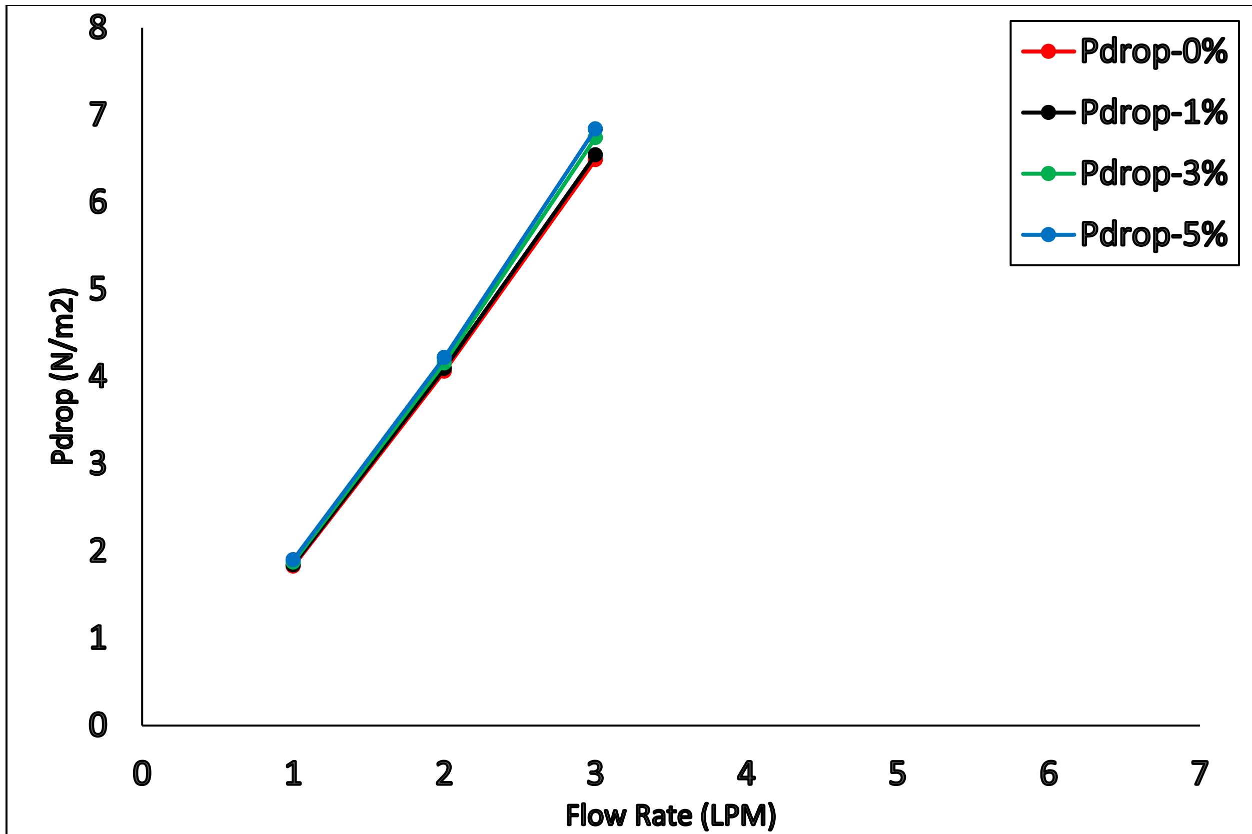

Figure 4-6: Variation of Pdrop with flow rate at different mass% of Al2O3 for plate fin heatsink geometry

Figure 4-6 shows the variation of pressure drop with flow rates of 1, 2 and 3 LPM, for 0, 1, 3 and 5 mass% of Al2O3 for the plate fin heatsink configuration. The pressure drop increases exponentially with flow rate, from a maximum value of 1.90 N/m2 to 6.84 N/m2 for 5 mass% concentration of Al2O3. At 0 mass% concentration of Al2O3, the increase in pressure drop is 4.66 N/m2, from 1.82 to 6.48 N/m2. The increment in pressure drop of only 0.08 N/m2 is obtained at 1 LPM flow rate, from 0 to 5 mass% of Al2O3, which is negligible, compared to a change of 0.36 N/m2 at 3 LPM flow rate. Hence, maximum drop in CPU Tmax with least reduction in Pdrop is obtained at 1 LPM flow rate, from a mass% of 0 to 5.

4.4 Pumping Power for the 3 Heatsink geometries:

Pumping power is calculated based from the following equation:

$$P = Q\Delta P \quad (10)$$

Where, ΔP is the pressure drop in N/m2 and Q is the flow rate in m3/s, and P is the pumping power in W.

Table 8**:** Pumping Power for the parallel plate heatsink geometry:

Configuration	Flow Rate (Q) (LPM)	Concentration %	Pumping Power Q×ΔP $\times 10^{-4}$ (W)
Parallel Plate	1	0	**0.49**
	2		**2.19**
	3		**5.25**
	1	1	**0.50**
	2		**2.22**
	3		**5.30**
	1	3	**0.51**
	2		**2.25**
	3		**5.38**
	1	5	**0.52**
	2		**2.29**
	3		**5.46**

Table 9**:** Pumping Power for the pin fin heatsink geometry:

Configuration	Flow Rate (Q) (LPM)	Concentration %	Pumping Power Q×ΔP $\times 10^{-4}$ (W)
Pin Fin	1	0	**0.19**
	2		**0.86**
	3		**2.05**
	1	1	**0.19**
	2		**0.86**
	3		**2.07**
	1	3	**0.20**
	2		**0.88**
	3		**2.10**
	1	5	**0.20**
	2		**0.89**
	3		**2.14**

Table 10**:** Pumping Power for the plate fin heatsink geometry:

Configuration	Flow Rate (Q) (LPM)	Concentration %	Pumping Power Q×ΔP $\times 10^{-4}$ (W)
Plate Fin	1	0	**0.30**
	2		**1.35**
	3		**3.24**
	1	1	**0.31**
	2		**1.36**
	3		**3.27**
	1	3	**0.32**
	2		**1.38**
	3		**3.37**
	1	5	**0.32**
	2		**1.40**
	3		**3.42**

Tables 8, 9 and 10 show the pumping power for the three heatsink geometries at flow rates of 1, 2 and 3 LPM, for 0, 1, 3 and 5 mass% of Al2O3 in pure mineral oil. Out of the 3 chosen heatsink geometries for the study, simulations conducted for the case of the parallel plate heatsink configuration exhibited the highest wattage of pumping power, and least values of pumping power were obtained from the pin fin heatsink configuration. This can be accounted from the fact that the pressure drop builds up as the resistance to flow of the fluid increases. The large number of fins in the parallel plate heatsink configuration has a larger surface area, and creates larger resistance for the fluid flow, as opposed to the pin fin and plate fin heatsink geometries. At larger flow rates, increase in velocity for a constant inlet area results in the elevation of pressure drop. With increase in the mass% of Al2O3, the viscosity of Al2O3/Mineral Oil increases, thus elevating the pressure drop and the required pumping power

4.5 Percentage increase in pumping power for the 3 heatsink geometries between 0 and 5 mass% of Al2O3:

Table 11: Percentage increase in pumping power for the 3 heatsink geometries

Configuration	Flow Rate (Q) (LPM)	% ΔPumping Power
Parallel Plate	**1**	**6.12**
	2	**4.56**
	3	**4.00**
Pin Fin	**1**	**5.26**
	2	**3.48**
	3	**4.39**
Plate Fin	**1**	**6.66**
	2	**3.70**
	3	**5.55**

Table 11 shows the percentage increase in pumping power between 0 and 5 mass% of Al2O3 in Mineral. As tabulated, the highest increase in the pumping power is obtained in the case of plate fin heatsink geometry, at a flow rate of 1 LPM. The least increment in pumping power of 3.48% is obtained in the case of pin fin heatsink geometry, for 2 LPM

flow rate. Higher increments in the pumping power are observed at 1 LPM flow rate, with the pin fin heatsink configuration showing the least percentage increase in the flowrate, out of the 3 chosen heatsink geometries.

Chapter 5

CONCLUSION AND FUTURE SCOPE

Winterfell immersion cooling was studied numerically using nanofluid (mineral oil + Al_2O_3) for different concentrations. Due to high viscosity of mineral oil, pressure drop and pumping dramatically increases by increasing the flowrate. Maximum temperature can be reduced at least by 6 °C by increasing the flowrate from 1 LPM to 3 LPM, however the pressure drop increases by 300%. Therefore, flow rate of 1 LPM is recommended for cooling. By adding the nano particles, temperature reduces by about 3.5 °C while the pressure drop increases by just 4%. Amongst the simulated geometries, pin fin heat sink has the lowest pumping power (50% lesser compared to parallel plate heat sink). Adding nanoparticles can increase pumping power by around 5.2%, however it can add 7% more capacity to remove heat. Hence using the pin fin heatsink geometry at 1 LPM with 5 percent concentration of Al_2O_3 in mineral oil for cooling is the most efficient solution for safe operation of the server and optimum power. This work can be further extended to find the minimum pumping power of operation by optimization of flow rate and inlet temperature. To validate the calculated properties, an experiment could be conducted for the measurement of the properties of the Al_2O_3/Mineral Oil Nanofluid at the chosen concentrations of Al_2O_3, and to validate the results obtained from numerical analysis, in the current study. The newer generation of the Winterfell server is Leopard, which consists of 2 CPUs with higher power densities. Simulations can be performed on this server to study the effect of cooling using Al_2O_3/Mineral Oil at different nanoparticle concentrations of Al_2O_3. For the safe functionality of the servers and electronic components, it is imperative to conduct studies on their reliability. This study can also be

extended to study the effects of nanoparticles on the reliability of the servers and equipment. Also, efficient inlet guide vanes to regulate the flow of the nanofluid for cooling the servers could be designed, to decrease the pumping power and flow rate of the nanofluid at the servers inlet. This could help subsidizing the cost of operation, and achieve the results of decrease in the maximum CPU temperature using nanofluids.

REFERENCES

[1] J. M. Shah, R. Dandamudi, C. Bhatt, P. Rachamreddy, P. Bansode, and D. Agonafer, “CFD Analysis of Thermal Shadowing and Optimization of Heatsinks in 3rd Generation Open Compute Server for Single-Phase Immersion Cooling.” Oct. 07, 2019, doi: 10.1115/IPACK2019-6600.

[2] P. A. Shinde *et al.*, “Experimental analysis for optimization of thermal performance of a server in single phase immersion cooling,” 2019, doi: 10.1115/IPACK2019-6590.

[3] J. M. Shah *et al.*, “Development of a technique to measure deliquescent relative humidity of particulate contaminants and determination of the operating relative humidity of a data center,” 2019, doi: 10.1115/IPACK2019-6601.

[4] G. Thirunavakkarasu, S. Saini, J. Shah, and D. Agonafer, “Air flow pattern and path flow simulation of airborne particulate contaminants in a high-density data center utilizing airside economization,” 2018, doi: 10.1115/IPACK2018-8436.

[5] S. Saini, P. Shahi, P. Bansode, A. Siddarth, and D. Agonafer, “CFD Investigation of Dispersion of Airborne Particulate Contaminants in a Raised Floor Data The University of Texas at Arlington 701 S Nedderman Drive,” 2011.

[6] O. Awe, J. M. Shah, D. Agonafer, P. Singh, N. Kannan, and M. Kaler, “Experimental Description of Information Technology Equipment Reliability Exposed to a Data Center Using Airside Economizer Operating in Recommended and Allowable ASHRAE Envelopes in an ANSI/ISA Classified G2 Environment,” *J. Electron.*

Packag., vol. 142, no. 2, pp. 1–9, 2020, doi: 10.1115/1.4046556.

[7] S. Ramdas, P. Rajmane, T. Chauhan, A. Misrak, and D. Agonafer, "Impact of immersion cooling on thermo-mechanical properties of PCB's and reliability of electronic packages," 2019, doi: 10.1115/IPACK2019-6568.

[8] S. Zimmermann, I. Meijer, M. K. Tiwari, S. Paredes, B. Michel, and D. Poulikakos, "Aquasar: A hot water cooled data center with direct energy reuse," *Energy*, vol. 43, no. 1, pp. 237–245, 2012, doi: 10.1016/j.energy.2012.04.037.

[9] P. V. Bansode *et al.*, "Measurement of the thermal performance of a single-phase immersion cooled server at elevated temperatures for prolonged time," *ASME 2018 Int. Tech. Conf. Exhib. Packag. Integr. Electron. Photonic Microsystems, InterPACK 2018*, no. August, 2018, doi: 10.1115/IPACK2018-8432.

[10] E. Baker, "Liquid Immersion Cooling of Small," vol. 12, no. 1, pp. 163–173, 1973.

[11] A. Kampl, "Bitcoin 2-Phase Immersion Cooling and the Implications for High Performance Computing," 2014.

[12] P. A. Shinde *et al.*, "Experimental analysis for optimization of thermal performance of a server in single phase immersion cooling," 2019, doi: 10.1115/IPACK2019-6590.

[13] J. M. Shah *et al.*, "Development of a technique to measure deliquescent relative humidity of particulate contaminants and determination of the operating relative humidity of a data center," 2019, doi: 10.1115/IPACK2019-6601.

[14] G. Thirunavakkarasu, S. Saini, J. Shah, and D. Agonafer, "Air flow pattern and path flow simulation of airborne particulate contaminants in a high-density data center

utilizing airside economization," 2018, doi: 10.1115/IPACK2018-8436.

[15] "Server immersion cooling," [Online]. Available: https://en.wikipedia.org/wiki/Server_immersion_cooling.

[16] D. Gandhi *et al.*, "Computational analysis for thermal optimization of server for single phase immersion cooling," 2019, doi: 10.1115/IPACK2019-6587.

[17] P. V. Bansode *et al.*, "Measurement of the Thermal Performance of a Custom-Build Single-Phase Immersion Cooled Server at Various High and Low Temperatures for Prolonged Time," *J. Electron. Packag.*, vol. 142, no. 1, Mar. 2020, doi: 10.1115/1.4045156.

[18] S. Ramdas, P. Rajmane, T. Chauhan, A. Misrak, and D. Agonafer, "Impact of immersion cooling on thermo-mechanical properties of PCB's and reliability of electronic packages," 2019, doi: 10.1115/IPACK2019-6568.

[19] B. Kanimozhi and B. R. R. Bapu, "Experimental study of thermal energy storage in solar system using PCM," in *Advanced Materials Research*, 2012, vol. 433–440, pp. 1027–1032, doi: 10.4028/www.scientific.net/AMR.433-440.1027.

[20] R. Eiland, J. Fernandes, M. Vallejo, D. Agonafer, and V. Mulay, "Flow Rate and inlet temperature considerations for direct immersion of a single server in mineral oil," in *Thermomechanical Phenomena in Electronic Systems -Proceedings of the Intersociety Conference*, Sep. 2014, pp. 706–714, doi: 10.1109/ITHERM.2014.6892350.

[21] P. E. Tuma, “The merits of open bath immersion cooling of datacom equipment,” in *Annual IEEE Semiconductor Thermal Measurement and Management Symposium*, 2010, pp. 123–131, doi: 10.1109/STHERM.2010.5444305.

[22] P. & M. T. S. Components and Institute of Electrical and Electronics Engineers., *Proceedings of the Fifteenth InterSociety Conference on Thermal and Thermomechanical Phenomena in Electronic Systems : ITherm 2016 : May 31 - June 3, 2016, Las Vegas, NV USA*. .

[23] Bansode, Pratik V., Shah, Jimil M., Gupta, Gautam, Agonafer, Dereje, Patel, Harsh, Roe, David, and Tufty, Rick. "Measurement of the Thermal Performance of a Single-Phase Immersion Cooled Server at Elevated Temperatures for Prolonged Time." *Proceedings of the ASME 2018 International Technical Conference and Exhibition on Packaging and Integration of Electronic and Photonic Microsystems*. San Francisco, California, USA. August 27–30, 2018. V001T02A010. ASME.

[24] S. Lee, -S Choi, S. Li, and J. A. Eastman, “Measuring Thermal Conductivity of Fluids Containing Oxide Nanoparticles,” 1999. [Online]. Available: http://heattransfer.asmedigitalcollection.asme.org/.

[25] J. M. Shah, R. Dandamudi, C. Bhatt, P. Rachamreddy, P. Bansode, and D. Agonafer, “CFD Analysis of Thermal Shadowing and Optimization of Heatsinks in 3rd Generation Open Compute Server for Single-Phase Immersion Cooling.” Oct. 07, 2019, doi: 10.1115/IPACK2019-6600.

[26] U. Rea, T. McKrell, L. wen Hu, and J. Buongiorno, “Laminar convective heat transfer and viscous pressure loss of alumina-water and zirconia-water nanofluids,” *Int. J. Heat Mass Transf.*, vol. 52, no. 7–8, pp. 2042–2048, Mar. 2009, doi: 10.1016/j.ijheatmasstransfer.2008.10.025.

[27] E. Ebrahimnia-Bajestan, M. Charjouei Moghadam, H. Niazmand, W. Daungthongsuk, and S. Wongwises, “Experimental and numerical investigation of nanofluids heat transfer characteristics for application in solar heat exchangers,” *Int. J. Heat Mass Transf.*, vol. 92, pp. 1041–1052, Jan. 2016, doi: 10.1016/j.ijheatmasstransfer.2015.08.107.

[28] Z. Y. Ghale, M. Haghshenasfard, and M. N. Esfahany, “Investigation of nanofluids heat transfer in a ribbed microchannel heat sink using single-phase and multiphase CFD models,” *Int. Commun. Heat Mass Transf.*, vol. 68, pp. 122–129, Nov. 2015, doi: 10.1016/j.icheatmasstransfer.2015.08.012.

[29] W. Duangthongsuk and S. Wongwises, “Heat transfer enhancement and pressure drop characteristics of TiO2-water nanofluid in a double-tube counter flow heat exchanger,” *Int. J. Heat Mass Transf.*, vol. 52, no. 7–8, pp. 2059–2067, Mar. 2009, doi: 10.1016/j.ijheatmasstransfer.2008.10.023.

[30] K. S. Hwang, S. P. Jang, and S. U. S. Choi, “Flow and convective heat transfer characteristics of water-based Al2O3 nanofluids in fully developed laminar flow regime,” *Int. J. Heat Mass Transf.*, vol. 52, no. 1–2, pp. 193–199, Jan. 2009, doi:

10.1016/j.ijheatmasstransfer.2008.06.032.

[31] J. Y. Jung, H. S. Oh, and H. Y. Kwak, “Forced convective heat transfer of nanofluids in microchannels,” *Int. J. Heat Mass Transf.*, vol. 52, no. 1–2, pp. 466–472, Jan. 2009, doi: 10.1016/j.ijheatmasstransfer.2008.03.033.

[32] J. Y. Jung, H. S. Oh, and H. Y. Kwak, “Forced convective heat transfer of nanofluids in microchannels,” *Int. J. Heat Mass Transf.*, vol. 52, no. 1–2, pp. 466–472, Jan. 2009, doi: 10.1016/j.ijheatmasstransfer.2008.03.033.

[33] A. Niazmand, Fathi Sola, J.Alinejad, F.; Rahimi Dehgolan, F.Investigation of mixed convection in a cylindrical lid driven cavity filled with water-cu nanofluid. *Inventions*, 2019,4,60.

[34] B. G. Dehkordi, S. Fallah, and A. Niazmand, “Investigation of harmonic instability of laminar fluid flow past 2D rectangular cross sections with 0.5-4 aspect ratios,” *Proc. Inst. Mech. Eng. Part C J. Mech. Eng. Sci.*, vol. 228, no. 5, pp. 828–839, 2014, doi: 10.1177/0954406213491906.

[35] Pardeep Shahi, Sarthak Agarwal, Satyam Saini, Amirreza Niazmand, Pratik Bansode, Dereje Agonafer, "CFD Analysis on liquid cooled cold plate using copper nanoparticles", ASME Conference Paper No. IPACK2020-2592

[36] Satyam Saini , Kaustubh K. Adsul, Pardeep Shahi, Amirreza Niazmand, Pratik Bansode, Dereje Agonafer, "CFD Modelling of the distribution of airborne particulate contaminants inside data center hardware", ASME Conference Paper No. IPACK2020-2590

[37] Amirreza Niazmand, Tushar Chauhan, Satyam Saini, Pardeep Shahi, Pratik Vithoba Bansode, Dereje Agonafer,"CFD Simulation of two-phase immersion cooling using FC-72 dielectricfluid". ASME Conference Paper No. IPACK2020-2595

[38] Amirreza Niazmand, Prajwal Murthy, Satyam Saini, Pardeep Shahi, Pratik Vithoba Bansode, Dereje Agonafer,"Numerical Analysis of Oil Immersion Cooling on a Server using Al2O3/Mineral Oil Nanofluid". ASME Conference Paper No. IPACK2020-2595